

Received 8 May 2023, accepted 21 May 2023, date of publication 24 May 2023, date of current version 5 June 2023.

Digital Object Identifier 10.1109/ACCESS.2023.3279725

## RESEARCH ARTICLE

# A Flexible mmWave Layer 2 Protocol Implementation for Integrated Access and Backhaul Architecture

**RANDY VERDECIA-PEÑA**<sup>1,2</sup>, (Member, IEEE),  
**RODOLFO OLIVEIRA**<sup>3,4</sup>, (Senior Member, IEEE),  
**AND JOSÉ I. ALONSO**<sup>1,2</sup>, (Member, IEEE)

<sup>1</sup>Information Processing and Telecommunications Center, Universidad Politécnica de Madrid, 28040 Madrid, Spain

<sup>2</sup>ETSI de Telecomunicación, Universidad Politécnica de Madrid, 28040 Madrid, Spain

<sup>3</sup>Departamento de Engenharia Electrotécnica, FCT, Universidade Nova de Lisboa, 2829-516 Caparica, Portugal

<sup>4</sup>IT, Instituto de Telecomunicações, 1049-001 Lisbon, Portugal

Corresponding author: Randy Verdecia-Peña (randy.verdecia@upm.es)

This work was supported in part by the Spanish Ministry of Science, Innovation and Universities funded by MCIN/AEI/10.13039/501100011033 under Project PID2020-113979RB-C21; and in part by the Ministry of Economic Affairs and Digital Transformation and the European Union-NextGenerationEU under Project TSI-063000-2021-83 (DISRADIO). The work of Randy Verdecia-Peña was supported by the Ministry of Science and Innovation under Contract PRE2018-085032. The work of Rodolfo Oliveira was supported by *Fundação para a Ciência e Tecnologia* under Project UIDB/50008/2020 and Project 2022.08786.PTDC.

**ABSTRACT** In this paper, we present a 3GPP-inspired hardware implementation for the out-of-band Integrated Access and Backhaul (IAB) network, which serves as a solution to both coverage extension and capacity boosting in 5G and beyond networks. By employing an Ettus x310 software-defined radio (SDR) board, Pasternack's 60 GHz Transmitter (Tx) waveguide module, and Matlab<sup>TM</sup> software, we design and develop an easy-to-use out-of-band mmWave Layer 2 protocol. The proposed protocol decodes a frequency range 1 (FR1) 5G signal as input at 3.5 GHz, which is retransmitted to the UE as a frequency range 2 (FR2) 5G signal at 60 GHz. In the implementation of the Layer 2 protocol, the least squares (LS) estimator is adopted by considering the demodulation reference signal (DM-RS) and the channel state information reference signal (CSI-RS) as pilot symbols in real-world environments. To alleviate the performance degradation in the mmWave access link, a phase noise cancellation (PNC) algorithm based on the phase tracking reference signal (PT-RS) is implemented at the UE node where a PT-RS block structure is introduced in the mmWave Layer 2 protocol transmitter stage. We review and evaluate the key performance indicators (KPIs) of the proposed Layer 2 protocol in real non-line-of-sight (NLOS) environments and a comparison between the gNode-to-UE link is carried out. Our results indicate that the performance of the proposed Layer 2 protocol is similar to the obtained with the off-the-shelf equipment demonstrating the right functionality of the developed algorithms. Experimental results evidence the superiority of the proposed Layer 2 protocol over the gNodeB-to-UE link (direct link communication) and the best performance is obtained when the PNC algorithm is considered in the IAB architecture.

**INDEX TERMS** IAB architecture, Layer 2 protocol, phase noise cancellation, 60 GHz wireless testbench, measurements, performance evaluation.

## I. INTRODUCTION

Cellular networks will be able to support the growing applications and services demanded by the users in rural, urban, and

The associate editor coordinating the review of this manuscript and approving it for publication was Bilal Khawaja<sup>1</sup>.

high-speed environments with higher performance [1], [2]. In this context, 5G wireless communication networks are changing the mobile cellular paradigm into new scenarios and application services such as enhanced mobile broadband (eMBB) [3], [4], ultra-reliable and low-latency connection (URLLC) [5], [6], and massive machine-type

communications (MMTC) [7], [8], where high-performance and data-centric computing are required [9], [10]. The millimeter wave (mmWave) frequency band is enabling technology in 5G communication networks, being a topic of interest in recent years by the academia, standardization organizations, regulatory committees, and industry, as well as it is a key candidate for addressing the challenges of bandwidth shortage for 5G systems and beyond [11], [12], [13]. However, signals at mmWave bands undergo severe path loss and are highly sensitive to blockage as compared to frequency range 1 (FR1) of 5G [14], [15], [16], [17].

To solve the mmWave problem and as an evolution from 4G to 5G, a multi-hop backhauling architecture named Integrated Access and Backhaul (IAB) has been standardized to support data services through a wireless access link [18]. The simplest IAB network consists of three major components: IAB-donor (base station or gNodeB), IAB-node (relay node (RN)), and user equipment (UE). In this sense, the IAB network can also be known as a cooperative relaying with some advanced capabilities and the Decode-&-Forward (D&F) protocol is more suited for the RN of the IAB architecture, as considered in recent studies [19], [20].

IAB networks have motivated the research activity from the academy and industrial sectors. Although operating on mmWave or sub-6 GHz bands, the IAB architecture is playing an appreciable role in several practical environments in FR1 5G wireless communications, such as public safety networks [21], [22]. According to the 3GPP standard [18], IAB architectures can improve the spectral efficiency (SE) and reduce the communication delay without any requirement for the guard time/band in comparison with the standardized LTE relay nodes, however, the end-to-end packet delay may greatly increase due to the multi-hop transmission, so this limitation is one of the main aspects currently tackled in 3GPP Release-18, particularly for mobility scenarios [23]. Besides, the IAB architectures take advantage of the increased bandwidth available on mmWave systems [24], [25]. Another benefit is the higher flexibility in terms of wireless network deployment and configuration with respect to the 4G networks deployed in mmWave bands [26], [27].

Recently, several researchers focused on demonstrate the potential and challenges of the IAB architecture in 5G mmWave networks [28]. In [29], the authors presented the design of an in-band full duplex mmWave IAB architecture taking into account 3GPP features. To improve the network performance, the authors proposed an RF codebook design and RF effective channel estimation, a digital self-interference cancellation algorithm, and baseband beam-forming design. A mmWave over cable (mmWoC) architecture has been introduced in [30] allowing extend the effective indoor coverage under the IAB network. It is worthwhile to mention the amount of research involving theoretical aspects of the design of IAB architectures [24], [26], [27]. Besides, several works have studied the link-level simulation of the mmWave backhaul network and the hardware

implementation still constitutes a significant challenge [28], [31], [32]. It should be highlighted that the theoretical implementations and link-level simulations are really an important way for studying algorithms and architectures. Nevertheless, it is imperative that new research ideas can be developed and evaluated in real-world environments through wireless testbenches.

Recent research and development in the area of wireless communications using software-defined radio (SDR) platforms have been primordial in testing novel algorithms and network architectures allowing a faster evolution and deployment of the proofs-of-concept in the 5G communication networks [32], [33]. Furthermore, our research team has demonstrated the viability of employing the SDR together with Matlab<sup>TM</sup> software in the cooperative 5G network implementation [34]. However, from the mmWave hardware development, there are still too much practical challenges. In this context, a critical issue is the phase noise (PN) introduced by the local oscillator (LO) into the signal on both the transmitting and receiving sides, which has been shown to increase with the carrier frequency and is 20-40 times higher than for the FR1 [35], [36].

## A. CONTRIBUTIONS

In this paper, we focus on the improved system performance based on an IAB architecture using a wireless testbench. Therefore, based on the above motivation, we design and implement an out-of-band 60 GHz Layer 2 protocol IAB network using SDR boards, Matlab<sup>TM</sup> tools, and Pasternack's 60 GHz Transmitter (Tx) and Receiver (Rx) waveguide modules, allowing to help the communication between the source and destination nodes. The contributions of this paper include the following aspects:

- Development and implementation of the algorithms for hardware implementation of an out-of-band Layer 2 node taking into account the FR1 and FR2 5G downlink signals of the 3GPP standard in the backhaul link and access link, respectively.
- Layer 2 protocol implements frequency synchronization, error correction, search Cell-ID, and minimum mean square error (MMSE) equalization algorithm, allowing a practical correction of the received signal through the backhaul link.
- A practical least square (LS) channel estimator has been implemented at Layer 2 protocol considering two different physical channel reference signals standardized by the 3GPP as pilot symbols: demodulation reference signal (DM-RS) and channel state information reference signal (CSI-RS).
- To mitigate the phase noise in the mmWave UE side, we also implement the phase noise cancellation (PNC) algorithm standardized by the 3GPP using phase tracking reference signal (PT-RS) [37].
- From the hardware perspective, the proposed IAB mmWave testbench is comprised of USRPs from

National Instruments and Ettus, RF splitters, 60 GHz RF modules, and 60 GHz 24 dBi horn antennas from Pasternack. Matlab<sup>TM</sup> has been employed for the implementation of physical layer (PHY) signal processing, and media access control (MAC) layer in both FR1 and FR2 standards.

- Measurements campaigns and scenarios in indoor-to-indoor with non-line-of-sight (NLOS) environments are introduced, as well as descriptions of the node positions in the real-world scenarios and the main parameters of the 5G downlink signal.
- The impact of the LS estimator employing both DM-RS and CSI-RS pilot symbols is discussed according the measured error vector magnitude (EVM). Besides, we investigate the key performance indicators (KPIs) in the proposed mmWave Layer 2 IAB network in two NLOS scenarios, as well as a comparison with the direct link. Finally, the proposed testbench has been verified experimentally with Anritsu's Field Master Pro MS2090A high-performance spectrum and signal analyzer.

## B. OUTLINE

The rest of the paper is organized as follows. Section II discusses the IAB aspects already standardized by 3GPP for 5G NR and an overview of the IAB network in 5G advanced wireless communications in future 3GPP Release-18. In Section III, the system model of the proposed IAB architecture for the 5G network based on Layer 2 protocol is presented, and the channel estimation and phase noise compensation algorithms are introduced. Section IV introduces the design and implementation of the developed wireless testbench considering the proposed algorithms to implement the mmWave Layer 2 protocol and mmWave UE node. Section V details the measurements campaigns and Section VI analyses and compares the key performance indicators of the proposed IAB architecture with a traditional 5G network. At the end, the conclusions of this paper are drawn in Section VII.

## C. NOTATION

The set of complex number is denoted by  $\mathbb{C}$ . Lowercase boldface letters stand for vectors and uppercase boldface letters designate matrices. For a vector or matrix, we denote its conjugate, transpose, and conjugate transpose as  $(\cdot)^*$ ,  $(\cdot)^T$ , and  $(\cdot)^H$ , respectively. The  $N \times N$  identity matrix is denoted by  $\mathbf{I}_N$ . The statistical expectation operator, Hadamard product, and Frobenius norm are denoted as  $\mathbb{E}\{\cdot\}$ ,  $\odot$ , and  $\|\cdot\|_F$ , respectively.

## II. OVERVIEW OF IAB STANDARDIZATION

For many years, relay nodes have been a research topic that has generated a great deal of interest in industry and researchers. In early discussions about LTE, 3GPP defined the types of relaying technologies in the Release-10. However, due to the shortage of the existing LTE communication networks spectrum for backhaul, the LTE relay nodes

have been limited and restricted to a handful of commercial deployments in the 4G networks timeline. As an evolution of the relaying technologies, the 3GPP has standardized the IAB architecture in Release-16 [18], which enables the deployment of small cells without requiring additional backhaul infrastructure. Release-16 is centered around the physical layer specification and higher-layer protocols and architectures. This is defined with the intention of reusing existing 5G NR functions and interfaces, while also minimizing the impact on the core network [18]. It should be noted that the mmWave frequency band is the most significant feature introduced for the IAB architecture, enabling the use of a portion of the spectrum resources for the backhaul link and considering the massive beamforming technique [26], [27], [28].

The enhancements to Release-16 IAB was covered in the Release-17 work item on IAB improvements [38]. Release-17 focused on enhancing the IAB architecture in robustness, latency, spectral efficiency, and end-to-end performance. The IAB Release-17 work item had set an objective to enhance the capabilities of multiplexing transmissions between backhaul and access links. This involves enabling simultaneous distributed unit (DU) and mobile termination (MT) operation within an IAB node, providing extended possibilities for network communication. It should be noticed that these multiplexing options can improve IAB efficiency and reduce latency [28], [38]. Release-17 comprises several enhancements regarding topology adaptation, which includes improved robustness, load balancing, and reduced service interruption time. These improvements are aimed at strengthening the network's infrastructure, enhancing its capacity to handle traffic fluctuations, and minimizing service disruptions. To enhance backhaul robustness and efficiency in IAB-based deployments, Release-17 proposed topology redundancy allowing multiple parallel paths within the backhaul connectivity. This enables more general topology, routing, and transport enhancements, thereby improving the overall efficiency of the IAB deployment [26], [27], [28], [38].

In recent researchers [23], [39], the authors provide an overview of the approved work package for Release-18 (5G-Advanced) by 3GPP. This overview aims to provide a comprehensive understanding of the ongoing developments and innovations in 5G technology, such as flexible network topology that will exploit mobile IAB nodes and radio frequency (RF) smart repeaters. Firstly, to facilitate the deployment of mobile IAB nodes, Release-18 will define topology adaptation procedures and mobility enhancements for both IAB nodes and associated UEs. Additionally, measures for interference mitigation will also be specified to ensure optimal network performance. These developments aim to provide enhanced connectivity and mobility for users in a dynamic network environment [23], [39]. The 3GPP will conduct a study on RF repeaters to enhance their functionality within the network. As part of this study, RF repeaters will be capable of receiving management control information from the base station, including beamforming information,

and TDD configuration, among other features [23], [39]. By utilizing side control information such as beamforming information, UL-DL TDD configuration, and on-off control information, network-controlled repeaters can perform amplify-&-forward operation with better spatial directivity through beamforming, effectively mitigating unnecessary noise amplification [23], [39].

### III. MODEL SYSTEM

We consider a single-user (SU) downlink 5G transmission for an IAB architecture using a mmWave out-of-band Layer 2 protocol with a total number of  $K$  subcarriers taking into account the details of the 3GPP technical report in [40]. As depicted in Fig. 1, the system architecture consists of three nodes: one source (gNodeB), one IAB node (Layer 2 protocol), and a destination (UE). A source with  $N_T^S$  antennas and  $N_T^S$  RF transmit chains communicates  $N_s$  data streams to the IAB node. The Layer 2 protocol operates in half-duplex (HD) mode, which is equipped with  $N_R^R$  receive and  $N_T^R$  transmit antennas, as well as RF chains for the receive and transmit stages, respectively. The user is equipped with  $N_R^D$  antennas and  $N_R^D$  RF chains for reception.

At the source, let  $\mathbf{S} \in \mathbb{C}^{N_s \times K}$  represents the modulated data symbols matrix with  $\mathbb{E}\{\mathbf{S}\mathbf{S}^H\} = \mathbf{I}_{N_s}$ . After applying the baseband and RF precoding  $\mathbf{W} = \mathbf{M}_{ST}\mathbf{T} \in \mathbb{C}^{N_T^S \times N_s}$ , the transmitted signal from the gNodeB is given by

$$\mathbf{X} = \mathbf{W}\mathbf{S}, \quad (1)$$

where  $\mathbf{M}_{ST} \in \mathbb{C}^{N_T^S \times N_T^S}$  is an RF precoder implemented by two blocks: the first stage up-converts the baseband frequency to FR1 (in this work 3.5 GHz has been considered) band and the second one amplifies the transmitted 5G signal, as detailed in Section IV. The symbol  $\mathbf{T} \in \mathbb{C}^{N_T^S \times N_s}$  represents a digital baseband precoder. The power normalization in the transmitter is denoted by  $\|\mathbf{M}_{ST}\mathbf{T}\|_F^2 = KN_T^S$ . At the Layer 2 protocol, the receive signal can be written as

$$\mathbf{Y}_1 = \mathbf{H}_1\mathbf{X} + \mathbf{N}_1, \quad (2)$$

where  $\mathbf{H}_1 \in \mathbb{C}^{N_R^R \times N_T^S}$  denotes a gNodeB-to-Layer 2 protocol sub-6 GHz channel matrix and  $\mathbf{N}_1 \in \mathbb{C}^{N_R^R \times K}$  is the complex Gaussian noise matrix at the Layer 2 protocol with zero mean and covariance  $\mathbb{E}\{\mathbf{N}_1\mathbf{N}_1^H\} = \sigma_1^2\mathbf{I}_{N_R^R}$ , where  $\sigma_1^2$  describes the noise variance. Then, the received symbols are processed by a combiner  $\mathbf{M}_{RR} \in \mathbb{C}^{N_R^R \times N_R^R}$  followed by a baseband combiner  $\mathbf{R} \in \mathbb{C}^{N_R^R \times N_r}$ . It should be noticed that the decoding of the physical, control, and data channels, as well as channel estimation and equalization algorithm are performed in the combiner matrix taking into account the 3GPP standard [37], as detailed in the following subsections. Therefore, the estimated bits in the Layer 2 protocol ( $\hat{\mathbf{t}}$ ) are first modulated into M-QAM constellation symbols and mapped into  $N_r$  streams  $\hat{\mathbf{S}} = [\hat{\mathbf{S}}_1^T, \hat{\mathbf{S}}_2^T, \dots, \hat{\mathbf{S}}_{N_r-1}^T, \hat{\mathbf{S}}_{N_r}^T]^T \in \mathbb{C}^{N_r \times K}$ , where  $\hat{\mathbf{S}}_i$  is the  $i$ -th stream and  $(\cdot)^T$  describes the transpose operator. Thus, a baseband precoder  $\mathbf{F} \in \mathbb{C}^{N_T^R \times N_r}$  is applied to the  $N_r$  symbol streams, so obtaining  $N_T^R$  spatial symbol streams

$\mathbf{B} = [\mathbf{B}_1^T, \mathbf{B}_2^T, \dots, \mathbf{B}_{N_T^R-1}^T, \mathbf{B}_{N_T^R}^T]^T = \mathbf{F}\hat{\mathbf{S}} \in \mathbb{C}^{N_T^R \times K}$ . After that,

the precoded symbols streams  $\{\sum_{b=1}^{N_T^R} \mathbf{B}_b\}$  are converted into length- $K$  signals  $\{\sum_{k=1}^K \mathbf{B}_b[k]\}$  through a serial-to-parallel converter. Considering the Layer 2 protocol system model illustrated in Fig. 1, the OFDM signal in frequency domain is converted into OFDM symbols in time domain by means of an inverse fast Fourier transform (iFFT), which can be expressed as

$$v_b[l] = \frac{1}{\sqrt{K}} \sum_{k=0}^{K-1} \mathbf{B}_b[k] e^{j\frac{2\pi l k}{K}}, \quad (3)$$

where  $l = 0, 1, \dots, K-1$ . A cyclic prefix (CP) is added to the iFFT output in order to eliminate the interference caused by multipath propagation channel. The resulting time-domain  $N_T^R$  baseband signal streams are then up-converted to the mmWave frequency band by means of  $N_T^R$  RF chains ( $\mathbf{M}_{RT}$ ), where a component of phase noise ( $e^{j\theta_b^t[l]}$ ) is added as a multiplicative term due to the high oscillation frequency of mmWave transmitter and  $\theta_b^t[l]$  describes the rotation across subcarriers during  $l$ -th OFDM symbol in transmission. From the point of view of hardware implementation, the RF chains are implemented through a software-defined radio board and a mmWave Tx Pasternack unit [41], as described in Section IV.

The received signal at the destination can be written as

$$\mathbf{Y}_2 = \mathbf{H}_2\Theta^t\mathbf{V} + \mathbf{N}_2, \quad (4)$$

where  $\mathbf{H}_2 \in \mathbb{C}^{N_R^D \times N_T^R}$  is the 60 GHz-mmWave channel matrix between the Layer 2 protocol and UE node transporting  $N_r \times K$  signals,  $\Theta^t \in \mathbb{C}^{N_T^R \times N_T^R}$  is a diagonal matrix formed by the spectral phase noise components,  $\mathbf{V} = \mathbf{M}_{RT}\mathbf{B} \in \mathbb{C}^{N_T^R \times K}$  is the transmitted signal from the Layer 2 protocol freedom of phase noise and derived from (3), and  $\mathbf{N}_2 \in \mathbb{C}^{N_R^D \times K}$  is the complex Gaussian noise matrix at the destination node with zero mean and covariance  $\mathbb{E}\{\mathbf{N}_2\mathbf{N}_2^H\} = \sigma_2^2\mathbf{I}_{N_R^D}$ , where  $\sigma_2^2$  describes the noise variance. At the UE node, the incoming signals in (4) are received by  $N_R^D$  antennas, which are down-converted to baseband through  $N_R^D$  RF chains where the phase noise at the destination is introduced and defined as  $e^{j\theta_a^r[l]}$ . In phase noise term,  $\theta_a^r[l]$  denotes the rotation across subcarriers during  $l$ -th OFDM symbol in reception. Thus, the CP is removed and the OFDM demodulation is performed. Finally, a baseband matrix  $\mathbf{G} \in \mathbb{C}^{N_d \times N_d}$  is applied and from (4) the estimated data can be written as

$$\begin{aligned} \tilde{\mathbf{Y}}_2 &= \mathbf{G}^H \Theta^r \mathbf{M}_{DR}^H \mathbf{Y}_2 \\ &= \mathbf{G}^H \Theta^r \mathbf{M}_{DR}^H (\mathbf{H}_2 \Theta^t \mathbf{V} + \mathbf{N}_2) \\ &= \mathbf{G}^H \Theta^r \mathbf{M}_{DR}^H \mathbf{H}_2 \Theta^t \mathbf{V} + \mathbf{G}^H \Theta^r \mathbf{M}_{DR}^H \mathbf{N}_2 \\ &= \tilde{\mathbf{S}} + \tilde{\mathbf{N}}_2, \end{aligned} \quad (5)$$

where  $\tilde{\mathbf{S}} = \mathbf{G}^H \Theta^r \mathbf{M}_{DR}^H \mathbf{H}_2 \Theta^t \mathbf{V} \in \mathbb{C}^{N_d \times K}$  represents the desired signal streams and  $\tilde{\mathbf{N}}_2 = \mathbf{G}^H \Theta^r \mathbf{M}_{DR}^H \mathbf{N}_2 \in \mathbb{C}^{N_d \times K}$  term represents the noise in the access link. From (5),



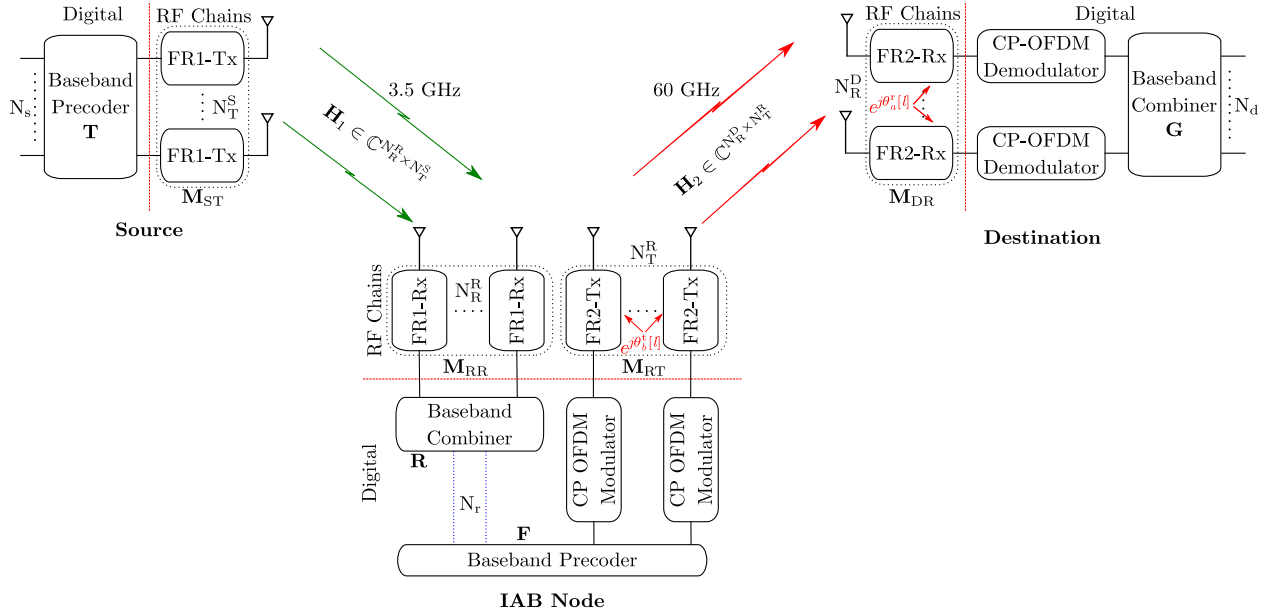


**FIGURE 1.** Simplified hardware block diagram of out-of-band mmWave Layer 2 protocol in the IAB architecture with transmitted and received phase noises.

$\Theta^r \in \mathbb{C}^{N_R^D \times N_R^D}$  denotes a diagonal matrix, whose diagonal entries are  $\{e^{j\theta_a^r[l]} | a = 1, 2, \dots, N_R^D\}$ ,  $\mathbf{M}_{DR} \in \mathbb{C}^{N_R^D \times N_R^D}$  is an RF combiner capable of performing the down-conversion from 60 GHz frequency band to baseband. It should be highlighted that in wireless communications in the 60 GHz frequency band the large phase noise from the frequency synthesizer with phase locked loop (PLL) occurs, which in this work is considered in the 60 GHz Pasternack transceiver. Therefore, OFDM modulation schemes with M-QAM are degraded by phase noise as presented in the system model. In this sense, a phase noise compensation has been implemented in the  $\mathbf{G}$  combiner matrix taking into consideration block-type pilot symbols, as presented in Subsection III-B.

#### A. CHANNEL ESTIMATION IN THE LAYER 2 PROTOCOL WITH DM-RS AND CSI-RS

Consider the received signal in (2) and the block diagram in Fig. 2, at the Layer 2 protocol. Firstly, a down-conversion from the FR1 frequency band to baseband is performed. Consequently, a synchronization and timing offset compensation is done through cross-correlating the input signal with a reference waveform. After that, the cyclic prefix is removed and resultant samples are changed from serial to parallel signals. Thus, by performing a fast Fourier transform (FFT) on the received signal we get the relation

$$y_{1s}[l] = \sum_{k=0}^{K-1} Y_{1s}[k] e^{-\frac{j2\pi lk}{K}}. \quad (6)$$

Based on the 3GPP standard, pilot samples are added in the gNodeB for use in the channel estimation block, whose pilot signals are extracted from the frequency domain signal

as their positions are known to the receiver. Therefore, (2) is composed of data information and pilot symbols, so if we consider only the pilot samples in an OFDM symbol, (2) is now written as

$$\mathbf{Y}_{1p}[s, k] = \mathbf{H}_{1p}[s, k] \mathbf{X}_p[s, k] + \mathbf{N}_{1p}[s, k], \quad (7)$$

where  $\mathbf{H}_{1p}[s, k]$  is the matrix of channel coefficients corresponding to pilot symbols,  $\mathbf{X}_p[s, k] \in \mathbb{C}^{P \times P}$  denotes the transmitted pilot symbols, and  $\mathbf{N}_{1p}[s, k]$  are the noise samples in frequency domain. The symbols  $s$  and  $k$  are the OFDM symbol index and the subcarrier index, respectively. Considering the LS estimator block, the LS channel estimation algorithm using (7) can be simply given by

$$\hat{\mathbf{H}}_{1p}[s, k] = \mathbf{X}_p^H[s, k] \mathbf{Y}_{1p}[s, k]. \quad (8)$$

In 5G NR, 3GPP has standardized the demodulation reference signals and the channel state information reference signal to be used as pilot symbols to facilitate channel estimation [37]. In this work both of DM-RS and CSI-RS pilot symbols have been implemented for estimating the propagation channel in the Layer 2 protocol. Consequently, based on [37], a sequence generation has been defined by

$$r(n) = \frac{1}{\sqrt{2}}[1 - 2c(2n)] + j \frac{1}{\sqrt{2}}[1 - 2c(2n + 1)], \quad (9)$$

where  $c(n)$  is a pseudo-random sequence of length-31 that can be written as

$$c(n) = [x_1(n + N_C) + x_2(n + N_C)] \bmod 2, \quad (10)$$

where  $N_C = 1600$ ,  $x_1(n + 31) = [x_1(n + 3) + x_1(n)] \bmod 2$ , and  $x_2(n + 31) = [x_2(n + 3) + x_2(n + 2) + x_2(n + 1) + x_2(n)] \bmod 2$ . Besides,  $\bmod$  represents the modulo operator

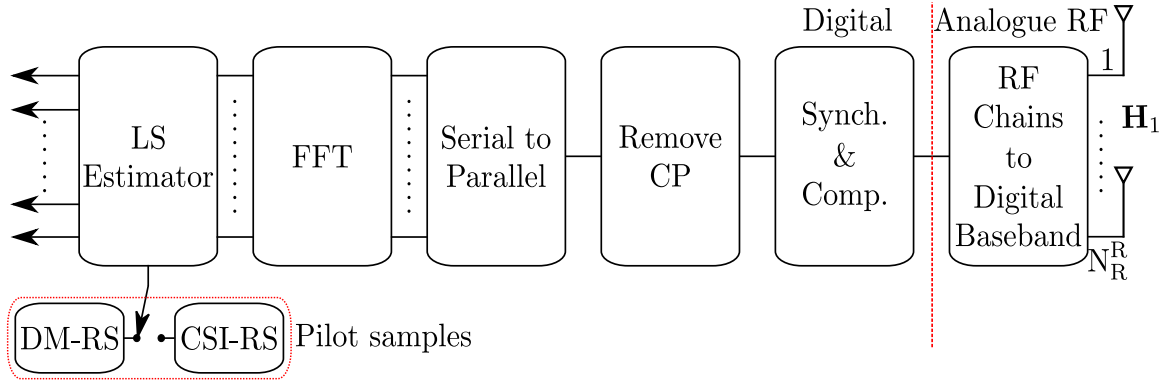


FIGURE 2. Block diagram for the pilot samples selection in the LS estimator on the Layer 2 protocol.

and the 31-first sequences  $x_1(n)$  and  $x_2(n)$  should be initialized, respectively, as follows

$$x_1(n) = \begin{cases} 1, & n = 0 \\ 0, & n = 1, 2, \dots, 30 \end{cases} \quad (11)$$

and

$$c_{init} = \sum_{i=0}^{30} x_2(i)2^i. \quad (12)$$

The value of  $c_{init}$  depends on the application and in our case is used estimating the wireless propagation channel using the DM-RS and CSI-RS. Therefore, when the DM-RS is implemented in the LS estimator block, the pseudo-random sequence generator is calculated by

$$c_{init}^{dmrs} = [2^{17}(N_n + s + 1)(2N_{ID}^{nscid} + 1) + 2N_{ID}^{nscid} + n_{SCID}] \bmod 2^{31}, \quad (13)$$

where  $N_n = N_{slot}^{slot} n_f^\mu$  with  $N_{slot}^{slot} = 14$  being the number of OFDM symbols in one slot,  $n_f^\mu = 10$  represents the slot number within a frame, and  $s$  describes the OFDM symbol index. On the other hand,  $N_{ID}^0, N_{ID}^1 \in \{0, 1, 2, \dots, 65535\}$ , and  $n_{SCID} \in \{0, 1\}$ .

Similarly, we also consider the CSI-RS pilot symbols to estimate the effect of the established propagation channel between the gNodeB and Layer 2 protocol. Thus, by assuming the sequence generation in (9), pseudo-random sequence in (10), and the  $x_1(n)$  initialization in (11), we can generate the CSI-RS signals considering the pseudo-random sequence generator  $c_{init}^{csirs}$  as [45]

$$c_{init}^{csirs} = [2^{10}(N_n + s + 1)(2n_{SCID} + 1) + n_{SCID}] \bmod 2^{31}, \quad (14)$$

where two types of CSI-RS pilot symbols have been defined in 3GPP [37], the first one zero-power (ZP) and the second one non-zero-power (NZP).

## B. PHASE NOISE CANCELLATION IN THE MMWAVE UE NODE

At the UE node, the obtained signal before the CP-OFDM demodulator and baseband combiner  $\mathbf{G}$  stages can be rewritten as

$$\hat{\mathbf{Y}}_2 = \Theta \odot \mathbf{Z}\mathbf{V} + \hat{\mathbf{N}}_2, \quad (15)$$

where  $\hat{\mathbf{N}}_2 = \Theta^H \mathbf{M}_{DR}^H \mathbf{N}_2$  is the additive noise (considers the inter-carrier-interference (ICI)),  $\mathbf{Z} = \mathbf{M}_{DR}^H \mathbf{H}_2$ ,  $\odot$  denotes the Hadamard product, and  $\Theta = \{\Theta_{a,b}\} \in \mathbb{C}^{N_R^D \times N_T^R}$  for convenience is given by [42] and [43]

$$\Theta_{a,b} = \frac{1}{K} \sum_{l=0}^{K-1} e^{j\theta_a^r[l]} \frac{1}{K} \sum_{l=0}^{K-1} e^{j\theta_b^t[l]} \approx e^{j(\tilde{\theta}_a^r + \tilde{\theta}_b^t)}, \quad (16)$$

where the approximation in (16) fits if the deviation in an OFDM symbol is very small, as demonstrated in [43]. In this sense,  $\tilde{\theta}_a^r$  and  $\tilde{\theta}_b^t$  describe the rotation across subcarriers during that OFDM symbol. To estimate the impact of phase noise that the local oscillator at the Layer 2 protocol and UE receiver have introduced, phase tracking reference signals have been implemented. The idea is to allocate a frequency contiguous block of this reference signal, allowing estimating phase noise introduced at the Layer 2 protocol (transmitter) and UE node (receiver), improving the link performance [44]. PT-RS allows the suppression of phase noise and common error, so according to (15) and assuming that the mmWave propagation channel is invariant during a slot, the received signals for subcarrier  $k$  in the  $d$ -th and  $s$ -th symbols with  $s > d$  can be written as

$$\hat{\mathbf{Y}}_2[d, k] = \Theta[d] \odot \mathbf{Z}[d, k] \mathbf{V}[d, k] + \hat{\mathbf{N}}_2[d, k] \quad (17)$$

and

$$\hat{\mathbf{Y}}_2[s, k] = \Theta[s] \odot \mathbf{Z}[s, k] \mathbf{V}[s, k] + \hat{\mathbf{N}}_2[s, k] \quad (18)$$

respectively. Therefore, considering the inserted total number of PT-RS pilot symbols  $M$ , the difference of phase error in

symbol  $d$  and  $s$  can be obtained as [45]

$$\hat{\theta} = \text{angle}\left\{\sum_{k=1}^M \hat{\mathbf{Y}}_2^*[d, k] \hat{\mathbf{Y}}_2[s, k]\right\}, \quad (19)$$

where  $\hat{\theta}$  is the rotating phase noise angle obtained using  $\Theta[d] \odot \mathbf{Z}[d, k]$  through the LS channel estimator, besides, we get the channel affected by the phase noise of all data symbols. Taking into account [37], the  $k$ -th PT-RS can be mapped in physical resources as

$$k = k_{\text{ref}}^{\text{RE}} + (iK_{\text{PT-RS}} + k_{\text{ref}}^{\text{RB}})N_{\text{sc}}^{\text{RB}}, \quad (20)$$

where  $i = 0, 1, 2, \dots, k_{\text{ref}}^{\text{RE}}$  is calculated for the DM-RS port associated with the PT-RS port,  $K_{\text{PT-RS}} \in \{2, 4\}$ ,  $N_{\text{RB}}$  is the resource block number allocated for the physical downlink shared channel transmission,  $N_{\text{sc}}^{\text{RB}}$  is the number of subcarriers per resource block, and  $k_{\text{ref}}^{\text{RB}}$  is given by

$$k_{\text{ref}}^{\text{RB}} = \begin{cases} n_{\text{RNTI}} \bmod K_{\text{PT-RS}} & \text{if } N_{\text{RB}} \bmod K_{\text{PT-RS}} = 0 \\ n_{\text{RNTI}} \bmod (N_{\text{RB}} \bmod K_{\text{PT-RS}}) & \text{otherwise,} \end{cases} \quad (21)$$

where  $n_{\text{RNTI}}$  is the radio network temporary identifier number associated with the downlink control information.

#### IV. HARDWARE PLATFORM

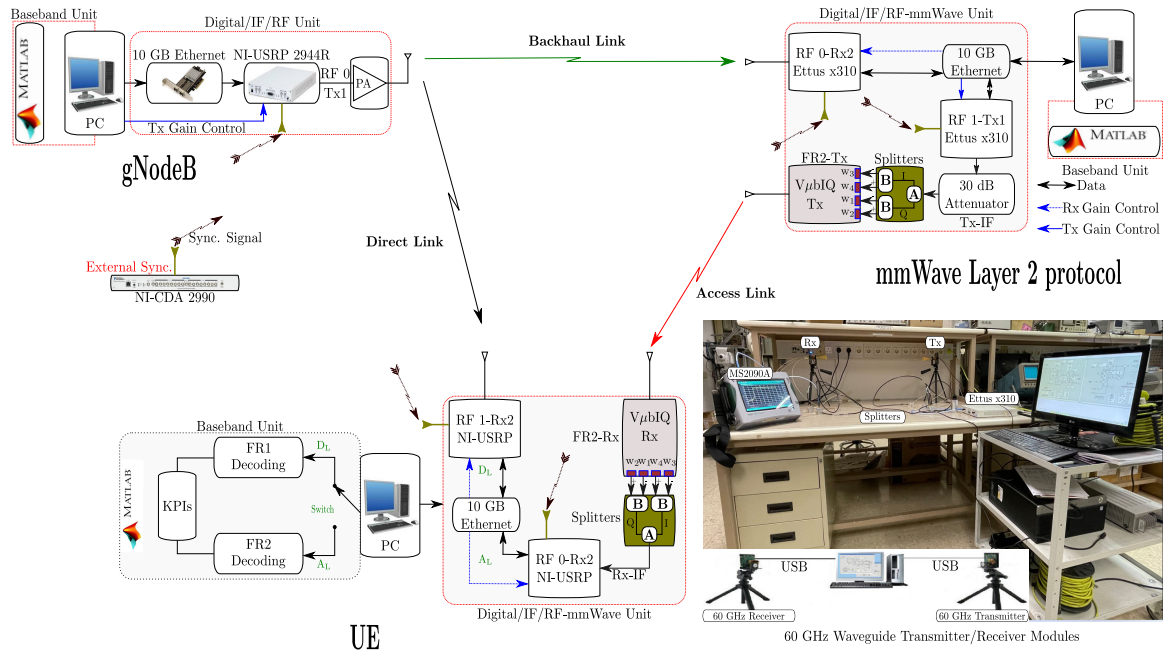
In this section, a hardware implementation testbench based on software-defined radio platform is proposed for the Layer 2 IAB network. It should be highlighted that the IAB standardization has been more focused on the adoption of mmWave FR2 bands in the backhaul link, nevertheless, it could also operate in sub-6 GHz FR1 frequency bands. Our work provides a sub-6 GHz band in the backhaul link and 60 GHz in the access link, as considered in [46] and [47]. However, in future lines of research, the authors will improve the proposed IAB platform to consider a 26 GHz backhaul link.

Fig. 3 shows the schematic diagram of hardware components. As shown in the figure, the software implementation of the proposed high-level architecture baseband unit for 60 GHz-mmWave Layer 2 IAB network has been written in Matlab<sup>TM</sup> using the 5G communication ToolBox. The proposed testbench comprises three major nodes: the gNodeB, the RN implementing the mmWave Layer 2 protocol, and the UE. On the gNodeB-side setup, one host PC generates the baseband 5G downlink signal using the Matlab<sup>TM</sup> software, which is routed to the NI-USRP 2944R for frequency up-conversion via 10 Gigabit ethernet cable. The connection between the PC and USRP is performed by means of the NI-IMAQdx GigE vision high-performance driver, a 10 Gigabit ethernet card for desktop, and 10 Gigabit ethernet cable. In addition, to the output of the USRP in the gNodeB we added the ZHL-1042J power amplifier (PA) to extend the coverage of the mmWave IAB network, as adopted in [48].

On the gNodeB hardware described above, we implemented a 5G downlink signal PHY to support the data symbols from the gNodeB to the Layer 2 protocol and UE node. We implemented a 64-QAM modulation scheme over 52 allocated resource blocks (RBs) (each RB contains 14 symbols in the time domain and 12 subcarriers in the frequency domain), and a subcarrier spacing of 15 kHz. In the CP-OFDM modulation, we used 1024 FFT points and a normal cyclic prefix corresponding to the 10 MHz of bandwidth of the emulated 5G signal. Furthermore, we have performed 20 transmissions, and in each transmission 80 frames are sent.

The mmWave Layer 2 protocol receives the transmitted 5G signal from the gNodeB at the carrier frequency  $F_c = 3.5$  GHz. This function is performed through the receiver stage of one x310 SDR, which is connected to another PC via 10 Gigabit ethernet cable. On the mmWave D&F strategy, we have developed the decoding and encoding stages (baseband unit) of the received signal through the implemented algorithms, which are detailed in Subsection IV-A. When the signal to re-transmit from the mmWave Layer 2 protocol is ready, it is sent to the UE by means of the mmWave Tx RF front-end. Then, the host PC is connected to the Tx stage of the x310 via a 10 Gigabit ethernet cable. The x310 platform is configured to Tx mode and converts the digital FR2 5G downlink signal to analog intermediate frequency (IF) signal to 470 MHz. The single I/Q waveform output of x310 is connected to the RF variable attenuator (50v70 SMA), which is fixed to 30 dB. After that, the attenuated signal is streamed to the mmWave stage through the ZFSCJ-2-S+ Power Splitter/Combiner (block A) to achieve the I (in-phase) and Q (quadrature) outputs. Then, I and Q components are up-converted to the 60 GHz unlicensed spectrum band through a V $\mu$ bIQ Pasternack 60 GHz Tx RF frontend [41]. The input of the Pasternack 60 GHz Tx RF frontend is connected to the differential I/Q signals obtained from the ZX10Q-2-3-S+ Power Splitter/Combiners (block B), operating from 220 MHz to 470 MHz, as presented in Fig. 3. Furthermore, the Pasternack Tx Unit is connected with a horn antenna by means of a WR-15 waveguide interface, and in this work the horn antenna has 24 dBi gain. The Pasternack Tx Unit is a commercially available 60 GHz front-end that can be configured through a universal serial bus (USB) interface connected to a host personal computer (PC) [41]. The software program allows choosing multiple parameters, for example, carrier frequency and the attenuation values. It should be highlighted that an external clock source is not necessary because the system provides an internal oscillation clocking operating at 308.571 MHz.

The UE-side consists of several sub-modules including sub-6 GHz/60 GHz mmWave down-converters and baseband processing, as depicted in Fig. 3. The proposed UE module considers both direct and access links to evaluate and demonstrate the benefits a Layer 2 protocol in 5G wireless communication. As depicted in Fig. 3, the UE-side captures the transmitted signal from the gNodeB when the switch is in the D<sub>L</sub> position. In this case, the physical layer



**FIGURE 3.** Hardware implementation testbench for Layer 2 IAB network and direct link between gNodeB-to-UE connection.

functionalities are implemented using the NI-USRP 2944R platform, specifically the RF1-Rx2 board. From the software environment, the  $D_L$  position activates the FR1 algorithms dedicated to the channel decoding, descrambling, demodulation, and de-mapping of the received 5G signal.

On the other hand, the UE implementation has the  $A_L$  position, which allows reserving the hardware resources and the baseband algorithms associated with the access link. As illustrated in Fig. 3, when  $A_L$  is established the I/Q signals transmitted by the mmWave Layer 2 protocol through the Pasternack Rx Unit are received. The Pasternack Rx Unit is an inverse connection of the Pasternack Tx Unit, where the horn antenna of 24 dBi of gain is connected to Pasternack 60 GHz RF frontend to convert the RF signal to the IF signal. Next, the differentials I/Q are combined through the splitters block, and the IF is then converted to the baseband 5G signal by one NI-USRP 2944R connected to the PC via a 10 Gigabit ethernet cable. Finally, the FR2 algorithm developed in Matlab<sup>TM</sup> performs the decoding of the received signal from mmWave Layer 2 protocol and obtains multiple metrics to evaluate the mmWave IAB architecture performance and to compare the relay link with the direct one.

### A. LAYER 2 PROTOCOL DESCRIPTION

In this subsection, we introduce the mmWave Layer 2 protocol implementation. Fig. 4 shows the schematic diagram of the proposed out-of-band mmWave D&F protocol. As shown in the figure, the first step is the radio frequency part which receives the signal from the BS through the RF 0-Rx2 of the Ettus x310 board. In Fig. 4, *NR Basic Structure* is the first block in the baseband processing having as inputs the

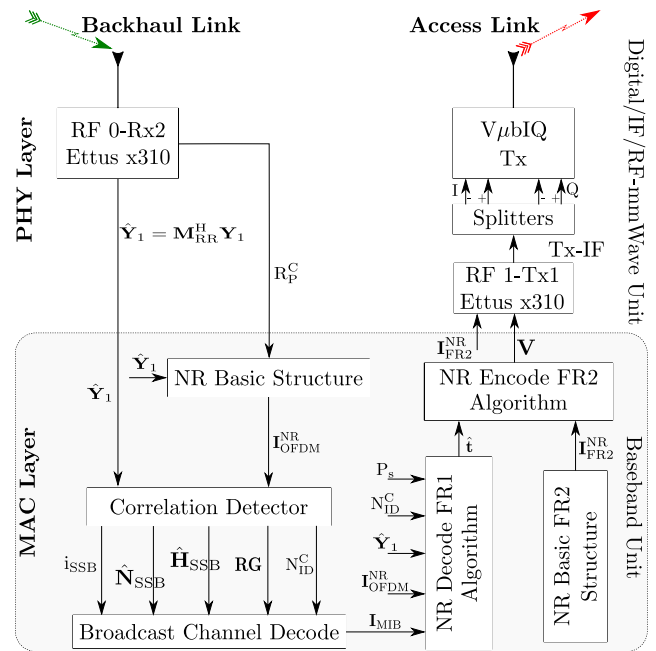


**FIGURE 4.** Schematic diagram of the proposed out-of-band mmWave Layer 2 protocol.

sample rate of the x310 board ( $\mathbf{R}_p^c$ ) and the received 5G signal after the Ettus x310 board ( $\hat{\mathbf{Y}}_1 = \mathbf{M}_{RR}^H \mathbf{Y}_1$ ). The output ( $\mathbf{I}_{OFDM}^{NR}$ ) contains the features of the received signal such as the cyclic prefix, the desired number of FFT points to use in the OFDM demodulator, and other information to start the signal synchronization.



For initial access, the out-of-band mmWave D&F protocol initiates the cell search procedure. Therefore, considering the primary synchronization signal (PSS), secondary synchronization signal (SSS), and developed synchronization algorithms, the D&F protocol can estimate and correct the frequency and time offsets in the *Correlation Detector* block, and the resultant waveform is defined as  $\mathbf{R}_x^{fc}$ . Layer 2 protocol flowchart detects the PSS reference signal, which consists of three 127-symbols  $m$ -sequences and it is allocated on the first symbol of each SSB and on 127 subcarriers. Thus, the three sector ID groups are computed through a cross-correlation operation and the sector ID group ( $N_{ID}^2$ ) with the highest correlation is selected. After decoding the PSS, the D&F protocol estimates and eliminates any significant frequency derivation, which allows decoding the SSS reference signal and the detection of the Cell ID group  $N_{ID}^1$  using the detected sector ID group  $N_{ID}^2$ . It should be noticed that the above procedures are also performed into the *Correlation Detector* block.

Taking into consideration  $N_{ID}^1$  and  $N_{ID}^2$ , the proposed 60 GHz-mmWave protocol can compute the serving physical Cell ID ( $N_{ID}^C$ ) and so identifies the candidate SSB within the SS burst. In addition, once demodulated the corrected received signal in time/frequency ( $\mathbf{R}_x^{fc}$ ) and detected  $N_{ID}^C$ , the resource grid ( $\mathbf{RG}$ ) resultant from CP-OFDM demodulation of the  $\mathbf{R}_x^{fc}$  signal is used to extract the PBCH DM-RS and is correlated with each reference PBCH DM-RS. It should be highlighted that the decoded DM-RS can be employed to estimate the reference signal received power (RSRP) of the detected SSB. Furthermore, it can be used for beam measurements. The estimated channel matrix ( $\hat{\mathbf{H}}_{SSB}$ ), estimated noise matrix ( $\hat{\mathbf{N}}_{SSB}$ ), and  $\mathbf{RG}$  are used to extract the received PBCH symbols from the SS/PBCH block and this step is implemented in the *Broadcast Channel Decode* block depicted in Fig. 4. Besides, MMSE equalization is performed on the PBCH symbols employing estimated channel and noise information after obtaining the subcarriers of the PBCH. Then, this block demodulates and descrambles the equalized PBCH symbols ( $\mathbf{RG}_{RE}^{PBCH}$ ). After that, the D&F protocol decodes the master information block ( $\mathbf{I}_{MIB}$ ), which is the output of the *Broadcast Channel Decode* block. So, after decoding, the protocol knows the sample timing within the full frame and can decode the full received signal ( $\hat{\mathbf{Y}}_1$ ).

Algorithm 1 performs the decoding of the control, reference, and data channels. The algorithm starts to resample to the nominal sampling rate and to adjust the timing offset to the frame origin by the  $\mathbf{T}_c^0(\cdot)$  function. The CP-OFDM demodulation on full bandwidth is realized by the  $\mathbf{nrCP}_d^{ofdm}(\cdot)$  function, where  $N_{ID}^C$ ,  $\mathbf{I}_{MIB}$ , and  $\mathbf{I}_{OFDM}^{NR}$  are required as input parameters. The decoding of the control and data channels are performed in each slot and  $N_{fr}$  and  $N_{sl}$  describe the frame and slot number, respectively. Therefore, the  $\mathbf{R}_x^{sub}$  matrix stores the resource grid slot temporarily depending on  $N_{fr}$  and  $N_{sl}$ . As explained in Subsection III-A, we designed and implemented a least square channel estimation over the data channel. In this work, two types of pilot samples are

#### Algorithm 1 NR Decode FR1 Algorithm.

---

**Input** :  $\hat{\mathbf{Y}}_1$ ,  $N_{ID}^C$ ,  $\mathbf{I}_{OFDM}^{NR}$ ,  $\mathbf{I}_{MIB}$ ,  $P_s$   
**Output**:  $\hat{\mathbf{t}}$   
 $\mathbf{R}_x^c = \mathbf{T}_c^0(\hat{\mathbf{Y}}_1, \text{frame}^{\text{offset}});$   
 $\mathbf{Y} = \mathbf{nrCP}_d^{ofdm}(\mathbf{R}_x^c, N_{ID}^C, \mathbf{I}_{MIB}, \mathbf{I}_{OFDM}^{NR});$   
 $\hat{\mathbf{t}} = []$  and  $N_{fr} = \text{size}(\mathbf{Y});$   
**for**  $n_{fr} \leftarrow 0 : N_{fr} - 1$  **do**  
     $\mathbf{R}_x^{fr} = \mathbf{Y}(:, (10 * s_s^p * n_{fr} + 1) : (n_{fr} + 1) * 10 * s_s^p, :);$   
    **for**  $n_{sl} \leftarrow 0 : N_{sl}$  **do**  
         $\mathbf{R}_x^{sub} = \mathbf{R}_x^{fr}(:, (s_s^p * n_{sl} + 1) : (n_{sl} + 1) * s_s^p, :);$   
        Normalization of  $\mathbf{R}_x^{sub};$   
        **if**  $P_s == \text{dm-rs}$  **then**  
             $\mathbf{X}_p = \mathbf{NR-PDSCH}_{\text{sym}}^{\text{dm-rs}}(\mathbf{I}_{OFDM}^{NR}, \mathbf{I}_{MIB});$   
        **else**  
             $\mathbf{X}_p = \mathbf{NR-PDSCH}_{\text{sym}}^{\text{csi-rs}}(\mathbf{I}_{OFDM}^{NR}, \mathbf{I}_{MIB});$   
         $[\hat{\mathbf{H}}, \hat{\mathbf{N}}] = \mathbf{NR-LS}_{E_s}(\mathbf{R}_x^{sub}, \mathbf{X}_p);$   
         $\hat{\mathbf{Y}} = (\hat{\mathbf{H}}^H \hat{\mathbf{H}} + \hat{\mathbf{N}})^{-1} \hat{\mathbf{H}}^H \mathbf{R}_x^{sub};$   
         $[\text{dci}] = \mathbf{NR-PDCCH}^d(\hat{\mathbf{Y}}, \hat{\mathbf{H}}, \mathbf{I}_{MIB});$   
         $[\text{dlsch}^b, \text{pdsch}^s] = \mathbf{NR-PDSCH}^d(\hat{\mathbf{Y}}, \hat{\mathbf{H}}, \text{dci}, \mathbf{I}_{MIB});$   
         $[\text{data}^b] = \mathbf{NR-DLSC}^d(\text{dlsch}^b, \text{pdsch}^s, \mathbf{I}_{MIB});$   
         $[\hat{\mathbf{t}}] = \text{Cat}(\hat{\mathbf{t}}, \text{data}^b);$

---

proposed to perform the estimation of the propagation channel, one considers the channel state information reference signal, specifically, based on non-zero-power CSI-RSs with a density equal to 3; in the second one, the demodulation reference signals are also taken into account to estimate the backhaul link. It should be noticed that, the main idea behind these implementations is to determine the best pilot samples to achieve a good channel estimation and better performance in the Layer 2 protocol. In the implementation of the Layer 2 protocol, the designing and allocation of DM-RS and CSI-RS will be presented in Section V and fulfilled with the standardization of 3GPP (TS38.211). In Algorithm 1,  $P_s$  is the variable that defines which pilot samples will be employed for the LS estimator, so  $P_s = \text{dm-rs}$  selects the DM-RS pilot symbols and with  $P_s = \text{csi-rs}$  the CSI-RS pilots are considered. In order to minimize the effects of noise and channel distortion, Algorithm 1 implements the MMSE technique over  $\mathbf{R}_x^{sub}$  considering a single antenna.

After the steps described previously, Algorithm 1 is ready to decode the control and data downlink channels, as well as determining other reference signals in each time slot ( $N_{sl}$ ). It should be highlighted that the low-density parity-check (LDPC) method has been considered to decode the DL-SCH channel, which fulfills the 3GPP standard. Besides, in the proposed algorithm, the sub-index  $(\cdot)^d$  in the functions describes the processes of decoding. The the sub-index  $(\cdot)^b$  and  $(\cdot)^s$  in the output of the functions represent data bits and data symbols, respectively. Finally,  $\hat{\mathbf{t}}$  denotes the data

**Algorithm 2** NR Encode FR2 Algorithm.

---

```

Input :  $\hat{\mathbf{t}}, \mathbf{I}_{\text{FR2}}^{\text{NR}}$ 
Output:  $\mathbf{B}$ 
 $\mathbf{c} = \mathbf{E}_{\text{FR2}}^{\text{c}}(\mathbf{I}_{\text{FR2}}^{\text{NR}});$ 
 $\hat{\mathbf{S}} = [\ ];$ 
for  $n_{\text{fr}} \leftarrow 1 : N_{\text{fr}}$  do
  for  $n_{\text{sl}} \leftarrow 1 : N_{\text{sl}}$  do
     $\mathbf{c}.\text{nSlot} = n_{\text{sl}}$ 
     $\mathbf{c}.\text{nFrame} = n_{\text{fr}}$ 
     $[\text{dlsch}_{\text{tx}}^b] = \text{NR-DLSCH}^{\text{c}}(\hat{\mathbf{t}}, \mathbf{c}, \mathbf{I}_{\text{FR2}}^{\text{NR}});$ 
     $[\hat{\mathbf{S}}] = \text{NR-PDSCH}^{\text{c}}(\text{dlsch}_{\text{tx}}^b, \mathbf{c}, \mathbf{I}_{\text{FR2}}^{\text{NR}});$ 
   $[\text{pdccch}_{\text{tx}}^s] = \text{NR-PDCCH}^{\text{c}}(\mathbf{c}, \mathbf{I}_{\text{FR2}}^{\text{NR}});$ 
  Coreset and Search Space Configuration  $\rightarrow \mathbf{D}_{\text{s}}^{\text{c}}$ 
   $[\mathbf{b}] = \text{NR-P}^{\text{c}}(\text{dlsch}_{\text{tx}}^b, \hat{\mathbf{S}}, \mathbf{D}_{\text{s}}^{\text{c}});$ 
   $[\mathbf{B}] = \text{Cat}(\mathbf{B}, \mathbf{b});$ 
 $[\mathbf{B}] = \text{nrCP}_m^{\text{ofdm}}(\mathbf{B}, \mathbf{c}, \mathbf{I}_{\text{FR2}}^{\text{NR}});$ 
 $\text{ssb} = \text{NR} - \text{SSB}(\mathbf{c}, \mathbf{I}_{\text{FR2}}^{\text{NR}});$ 
 $[\mathbf{B}] = \mathbf{M}_{\text{c}}^{\text{ssb}}(\mathbf{B}, \text{ssb});$ 

```

---

bits vector estimated in Algorithm 1 and retransmitted to the destination using the Algorithm 2.

In the *NR Basic FR2 Structure* block, the FR2 5G signal parameters, and their default values are defined ( $\mathbf{I}_{\text{FR2}}^{\text{NR}}$ ). We adopt the 120 kHz subcarrier spacing of 5G numerologies, with 40 slots per frame, 4 slots per subframe, and 14 symbols per slot. The allocated resource blocks per frame are 66, with normal cyclic prefix, and 61.44 MHz of samples rate. We assume a frequency division 5G duplex scheme, in which the data channel uses Q-PSK modulation with 1/3 target code rate. Considering the above parameters, the implemented FR2 5G signal in the transmitting stage of the Layer 2 protocol has a 50 MHz channel bandwidth. As shown in Fig. 4,  $\mathbf{I}_{\text{FR2}}^{\text{NR}}$  is the output of the *NR Basic FR2 Structure* block, which carries all configuration parameters to perform the encode of data, control, reference signal, and physical channels, as well as the CP-OFDM modulation in Algorithm 2.

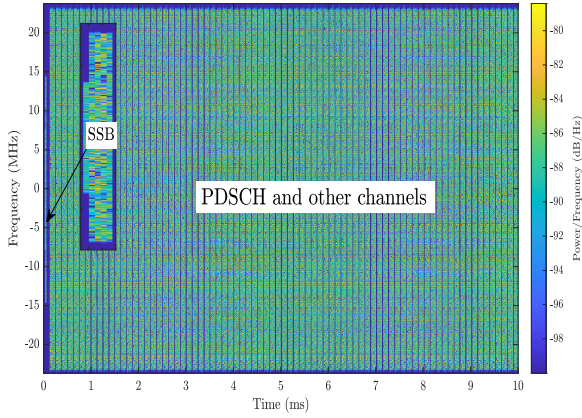
Based on the Layer 2 protocol defined by the 3GPP in the IAB architecture, the NR encoded FR2 signal is shown in Algorithm 2. In line 1, the algorithm is initialized with two input parameters:  $\hat{\mathbf{t}}$  stores all data bits that will be transmitted by the protocol and  $\mathbf{I}_{\text{FR2}}^{\text{NR}}$  provides all configuration to generate the FR2 signal. Furthermore, in line 3, the algorithm defines the  $\mathbf{E}_{\text{FR2}}^{\text{c}}(\cdot)$  function that extracts the set wave type and data channel numerology, thus identifying the subcarrier spacing and the CP type. More specifically, the  $\mathbf{c}$  structure supports the main configuration of the proposed algorithm. Given the defined variables, two steps are executed iteratively. The first step takes into account the number of frames retransmitted to the user equipment. In this step, the first task is to execute the second step that considers the number of slots per frame, in which the dlsch bits are obtained, and so are generated data symbols ( $\hat{\mathbf{S}}$ ) in each slot through the  $\text{NR} - \text{PDSCH}^{\text{c}}(\cdot)$  function. After that, the

control channel symbols are generated considering the  $\mathbf{I}_{\text{FR2}}^{\text{NR}}$  and  $\mathbf{c}$  configurations. The  $\text{NR} - \text{P}^{\text{c}}(\cdot)$  function maps each channel in the resource grid and  $\mathbf{b}$  stores the output subframes of the  $\text{NR} - \text{P}^{\text{c}}(\cdot)$  function. Accordingly, concatenating each subframe is performed by means of the  $\text{Cat}(\cdot)$  function, from which all frames retransmitting are saved.

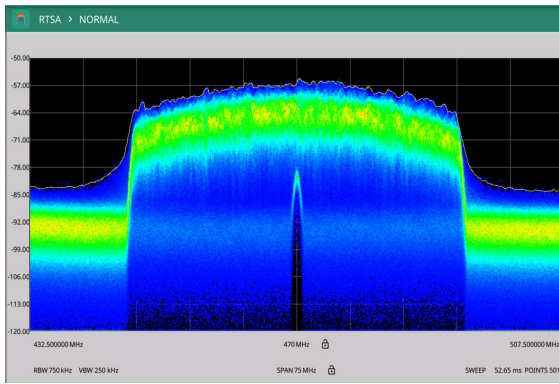
Finally, the  $\mathbf{B}$  is the resultant FR2 waveform that has been obtained through the  $\text{nrCP}_m^{\text{ofdm}}(\cdot)$ ,  $\text{NR} - \text{SSB}(\cdot)$ , and  $\mathbf{M}_{\text{c}}^{\text{ssb}}(\cdot)$  functions. The following step includes the hardware transmission implementation, as can be seen in the flowchart of the proposed Layer 2 protocol. Taking into account the hardware description in this section,  $\mathbf{B}$  is transmitted by the RF1-Tx1 Ettus x310 board, which has been configured to Tx mode and converts the digital retransmitted signal to analog intermediate frequency. The IF signal attacks one splitters chain, which achieves a differential I/Q that is connected to the input of Pasternack 60 GHz Tx RF frontend. From the matrices model, the transmitted signal to the output of the mmWave transmitter is given by  $\mathbf{V} = \mathbf{M}_{\text{RT}}\mathbf{B}$ .

Fig. 5 presents the spectrogram of the generated FR2 5G downlink baseband waveform to the output of the Algorithm 2. From Fig. 5, it is possible to observe the allocation of resource blocks in one frame (10 ms) and in the frequency domain it is possible to verify the 50 MHz bandwidth of the mmWave 5G signal implemented in the Layer 2 protocol to forward the decoded bits of the backhaul link to the UE node. Furthermore, the most important block for the synchronization between the Layer 2 protocol and the EU side is shown in the inset graph, which corresponds to the SS block that consists of four consecutive OFDM symbols with 240 subcarriers each. It should be noticed that the synchronization/PBCH block (SSB) is transmitted in a burst known as SS burst, which in our usage case is transmitted in each first half of a 10 ms frame as can be seen in Fig. 5. The block pattern implemented in the Layer 2 protocol is the *Case D* with the maximum number of beams equal to 64, however, in our development 1 SS burst has been exploited because the proposed platform has only one UE receiver. Besides, considering the 3GPP standard, one SSB with 120 kHz of subcarrier spacing has been configured, in which the first symbols of the designed SS/PBCH block have indexes  $\{4, 8, 16, 20\} + 28 \times n$  with  $n = [1, 2, \dots, 18]$ . On the other hand, the resource blocks that are allocated to other channels are visible in Fig. 5, for example, the data channel.

In order to evaluate the correct operation of the mmWave signal implemented in the Layer 2 protocol, several tests have been performed at the output of the 30 dB attenuator. Thus, Fig. 6 shows the real-time spectrum analyzer of the implemented FR2 signal through the Anritsu instrument. From the figure, we can conclude that the spectrum of the transmitted signal complies with the 3GPP requirements, where it is clearly defined in three zones: transmission bandwidth, OOB emission, and the far spurious domain. According to the 3GPP standard [40] and experimental tests carried out in our lab [48], a spectrum mask that does not be clearly defined significantly degrades system performance.



**FIGURE 5.** Representational figure illustrating the resource block allocation in a frame of the transmitted FR2 signal.



**FIGURE 6.** RTSA spectrum of the transmitted FR2 5G signal to the output of the x310 board in the Layer 2 protocol.

In Fig. 7, the SSB demodulation of the FR2 5G signal implemented in the Layer 2 protocol measured by the MS2090A Anritsu spectrum analyzer is presented. It can be seen on the left edge of the figure that the signal characteristics shown in the instrument correspond to those implemented in the FR2 signal (bandwidth = 50 MHz and subcarrier spacing = 120 kHz). Other data that demonstrate the right functioning are the green LEDs indicating that there is complete synchronization and demodulation between the transmitting side in the implemented protocol and the spectrum analyzer. For example, the EVM [%] of PSS and SSS are 0.90 and 0.80, respectively, and the EVM values of the PBCH and the demodulation reference signals associated with the PBCH are 3.09% and 0.16%, respectively.

The PBCH decoding is shown in the Fig. 8. The measurement from Fig. 8 validates that the EVM [%] of the broadcast channel is considerably low (3.06) in comparison with the requirements of the 3GPP [40]. The physical Cell ID = 0 of the Tx stage implemented in the Layer 2 protocol and its time and frequency offset have been detected and are perfectly correctable with the time and frequency offset correction algorithms developed in the UE node. Finally, from the figure, it can be corroborated that only one beam (0) has been activated as explained in Algorithm 2.

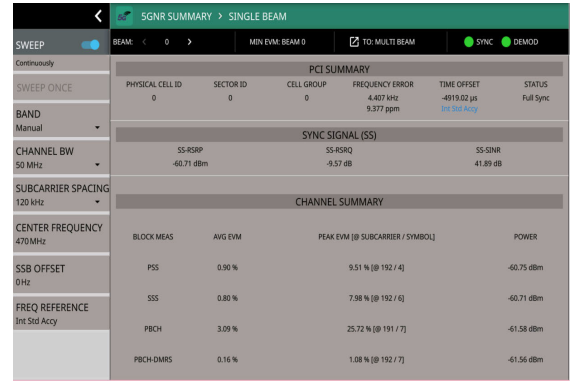


**FIGURE 7.** SSB demodulation of the transmitted FR2 5G signal to the output of the x310 board in the Layer 2 protocol.

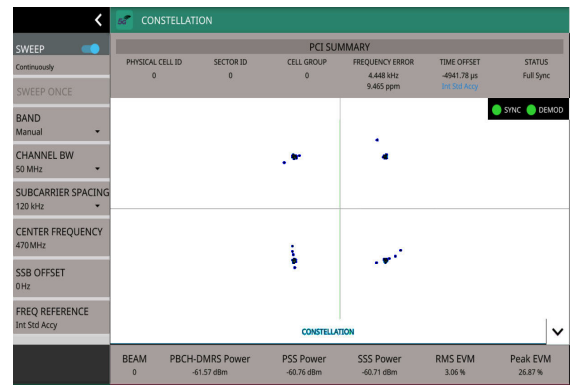


**FIGURE 8.** Constellation of the FR2 signal transmitted to the output of the x310 board in Layer 2 protocol.

## B. UE NODE IMPLEMENTATION

In this subsection, we present the UE node hardware implementation supporting 3.5 GHz and 60 GHz frequency bands. Fig. 9 shows the proposed block diagram of the UE node for the IAB network. In this implementation, we consider the PHY and MAC layers. From Fig. 9, it can be seen that the implementation is carried out in two stages, respectively, hardware and software steps. In addition, the UE node processes the 5G signal received from the gNode side and the Layer 2 protocol separately. The idea behind this approach is to demonstrate the benefits that can be introduced when the IAB architecture is employed in a 5G network.

Assuming that the *Link Selection* block determines which link is selected at the UE node. So, let  $L_s = D_L$ , in this case, the UE node will receive a 5G signal from the gNode side (direct link). From the hardware device, the RF 1-Rx2 side into the NI-2944R board is activated to receive the 3.5 GHz frequency band. Therefore, the baseband signal  $\hat{\mathbf{Y}}_{UE} = \hat{\mathbf{Y}}_3$  in the software stage is considered. The processed 5G signal ( $\hat{\mathbf{Y}}_3$ ) at the *Baseband Unit* block is given by

$$\hat{\mathbf{Y}}_3 = \tilde{\mathbf{M}}_{DR}^H (\mathbf{H}_3 \mathbf{X} + \mathbf{N}_3), \quad (22)$$

where  $\tilde{\mathbf{M}}_{DR}$  denotes the RF combiner that down-converts the received FR1 signal in the 3.5 GHz antenna to baseband



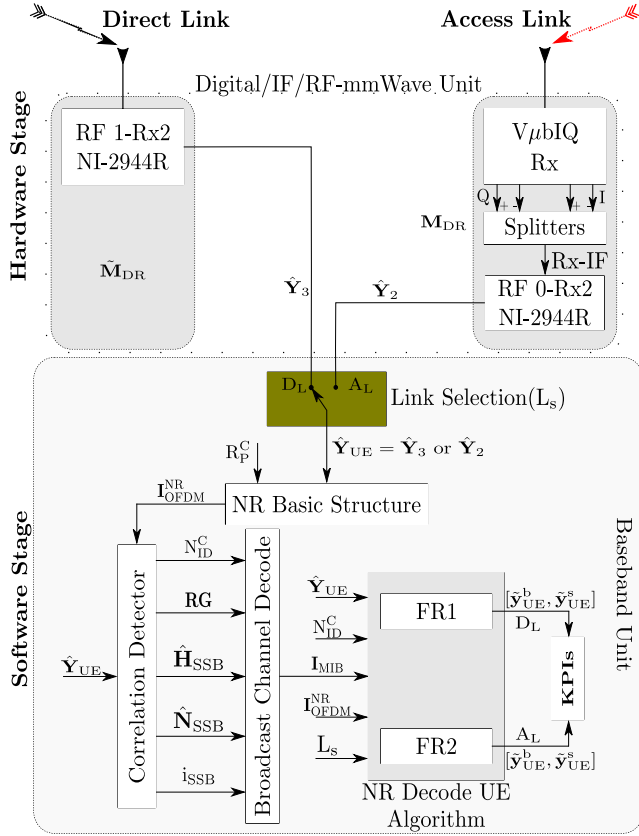


FIGURE 9. Block scheme of the proposed UE node with link selection.

frequency.  $\mathbf{H}_3$  is the channel matrix between the gNode and the destination node and  $\mathbf{N}_3$  is the noise matrix at the UE node. On the other hand, when  $L_s = A_L$  the UE node captures signal from the mmWave Layer 2 protocol as can be seen in Fig. 9. Thus, from hardware stage, the RF 0-Rx2 side in the NI-2944R is activated and the 60 GHz Pasternack Rx captures the mmWave signal from the Layer 2 protocol.

From the software stage, the output of *NR Basic Structure* block ( $\mathbf{I}_{\text{OFDM}}^{\text{NR}}$ ) is obtained depending on the  $L_s$  block. After that, the *Correlation Detector* and *Broadcast Channel Decode* blocks are processed. After the steps described previously, Algorithm 3 is executed taking into account the following inputs:  $\hat{\mathbf{Y}}_{\text{UE}}$  is the received signal after the RF combiner considering the *Link Selection* block, the detected physical Cell ID  $N_{\text{ID}}^{\text{C}}$ , the information of the master information block ( $\mathbf{I}_{\text{MIB}}$ ) got through the output of the *Broadcast Channel Decode* block, and the  $\mathbf{I}_{\text{OFDM}}^{\text{NR}}$  carries out the information to demodulated the OFDM received signal considering the *Link Selection* block. In Algorithm 3, it is firstly performed resampling to the nominal sampling rate and adjusted to the frame origin through the  $\mathbf{T}_c^o(\cdot)$  function. Once the received signal is corrected, full bandwidth CP-OFDM demodulation is performed using the  $\text{nrCP}_d^{\text{ofdm}}(\cdot)$  function. It can be seen in Algorithm 3 that the main loop processes the total number of demodulated frames ( $\mathbf{Y}$ ).

### Algorithm 3 NR Decode UE Algorithm With PNC.

**Input** :  $\hat{\mathbf{Y}}_{\text{UE}}, N_{\text{ID}}^{\text{C}}, \mathbf{I}_{\text{OFDM}}^{\text{NR}}, \mathbf{I}_{\text{MIB}}, L_s$   
**Output**:  $[\tilde{\mathbf{y}}_{\text{UE}}^b, \tilde{\mathbf{y}}_{\text{UE}}^s]$   
 $\mathbf{R}_x^c = \mathbf{T}_c^o(\hat{\mathbf{Y}}_{\text{UE}}, \text{frame}^{\text{offset}});$   
 $\mathbf{Y} = \text{nrCP}_d^{\text{ofdm}}(\mathbf{R}_x^c, N_{\text{ID}}^{\text{C}}, \mathbf{I}_{\text{MIB}}, \mathbf{I}_{\text{OFDM}}^{\text{NR}});$   
 $\tilde{\mathbf{y}}_{\text{UE}}^b = []$  and  $\tilde{\mathbf{y}}_{\text{UE}}^s = [];$   
 $N_{fr} = \text{size}(\mathbf{Y});$   
**for**  $n_{fr} \leftarrow 0 : N_{fr} - 1$  **do**  
  **if**  $L_s == A_L$  **then**  
     $\mathbf{R}_x^{\text{fr}} = \mathbf{Y}(:, (n_{fr}^{\mu} * s_s^p * n_{fr} + 1) : (n_{fr} + 1) * n_{fr}^{\mu} * s_s^p, :);$   
  **else**  
     $\mathbf{R}_x^{\text{fr}} = \mathbf{Y}(:, (n_f^{\mu} * s_s^p * n_{fr} + 1) : (n_{fr} + 1) * n_f^{\mu} * s_s^p, :);$   
  **for**  $n_{sl} \leftarrow 0 : N_{sl}$  **do**  
     $\mathbf{R}_x^{\text{sub}} = \mathbf{R}_x^{\text{fr}}(:, (s_s^p * n_{sl} + 1) : (n_{sl} + 1) * s_s^p, :);$   
    Normalization of  $\mathbf{R}_x^{\text{sub}};$   
     $\mathbf{S}_{\text{p}}^{\text{dm-rs}} = \text{NR-PDSCH}_{\text{sym}}^{\text{dm-rs}}(\mathbf{I}_{\text{OFDM}}^{\text{NR}}, \mathbf{I}_{\text{MIB}});$   
     $[\hat{\mathbf{H}}, \hat{\mathbf{N}}] = \text{NR-ES}(\mathbf{R}_x^{\text{sub}}, \mathbf{S}_{\text{p}}^{\text{dm-rs}});$   
     $\hat{\mathbf{Y}} = (\hat{\mathbf{H}}^H \hat{\mathbf{H}} + \hat{\mathbf{N}})^{-1} \hat{\mathbf{H}}^H \mathbf{R}_x^{\text{sub}};$   
    **if**  $L_s == A_L$  **then**  
       $[\mathbf{Z}_p, \hat{\mathbf{H}}_p] = \mathbf{E}_p^{\text{nr}}(\mathbf{R}_x^{\text{sub}}, \hat{\mathbf{H}});$   
       $\hat{\mathbf{Z}}_p = (\hat{\mathbf{H}}_p^H \hat{\mathbf{H}}_p + \hat{\mathbf{N}}_p)^{-1} \hat{\mathbf{H}}_p^H \mathbf{Z}_p;$   
       $[\mathbf{r}_{\text{nc}}^p] = \text{NR-ES}(\hat{\mathbf{Z}}_p, \mathbf{I}_{\text{ind}}^{\text{ptrs}}, \mathbf{I}_{\text{sym}}^{\text{ptrs}});$   
       $\hat{\theta} = \mathbf{An}(\mathbf{r}_{\text{nc}}^p);$   
      **for**  $k \leftarrow 1 : K$  **do**  
        **for**  $s \leftarrow 1 : N_{\text{slot}}^{\text{slot}}$  **do**  
           $\hat{\mathbf{Y}}_s^k(n_{sl}) = \hat{\mathbf{Y}}_s^k(n_{sl}) \times e^{-1j \times \hat{\theta}_s^k};$   
       $[\text{dci}] = \text{NR-PDCCH}^d(\hat{\mathbf{Y}}, \hat{\mathbf{H}}, \mathbf{I}_{\text{MIB}});$   
       $[\text{dlsch}^b, s^s] = \text{NR-PDSCH}^d(\hat{\mathbf{Y}}, \hat{\mathbf{H}}, \text{dci}, \mathbf{I}_{\text{MIB}});$   
       $[\mathbf{b}^b] = \text{NR-DLSCH}^d(\text{dlsch}^b, s^s, \mathbf{I}_{\text{MIB}});$   
       $[\tilde{\mathbf{y}}_{\text{UE}}^b] = \text{Cat}(\tilde{\mathbf{y}}_{\text{UE}}^b, \mathbf{b}^b);$   
       $[\tilde{\mathbf{y}}_{\text{UE}}^s] = \text{Cat}(\tilde{\mathbf{y}}_{\text{UE}}^s, s^s);$

In the main loop proposed in Algorithm 3, we extract one frame from  $\mathbf{Y}$  depending on whether direct link ( $D_L$ ) or access link ( $A_L$ ) is selected. Thus, the second main loop in algorithm considers the number of slot per frame. At this point, the DM-RS pilot symbols are extracted from the  $\mathbf{R}_x^{\text{sub}}$  slot, allowing the least squares channel estimation to be performed and, after that, the equalization is executed. Now, if the mmWave access link is considered, the proposed phase noise cancellation step is performed. As presented in Subsection III-B, the implemented PNC algorithm has been developed using PT-RS pilot samples as defined by the 3GPP standard that have been embedded in the retransmitted signal from the Layer 2 protocol. So,  $\mathbf{E}_p^{\text{nr}}(\cdot)$  function extracts the received PT-RS ( $\mathbf{Z}_p$ ) and the estimated channel ( $\hat{\mathbf{H}}_p$ ) associated to the PT-RS pilot samples in the slot  $n_{sl}$ . Using the MMSE



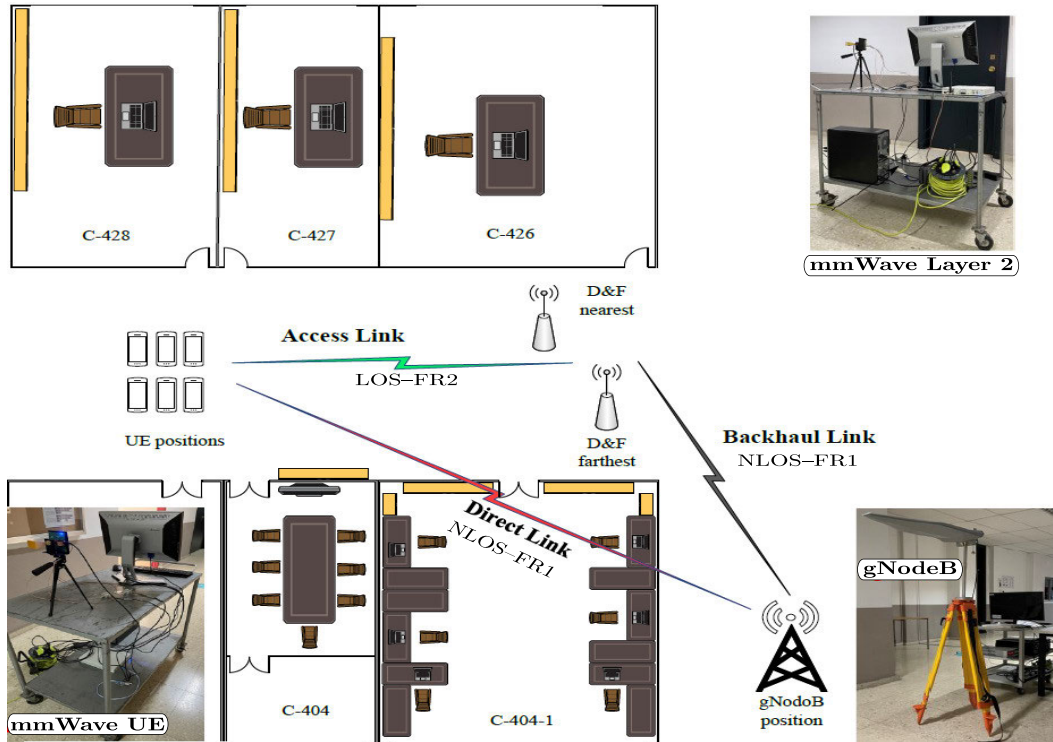


**FIGURE 10.** Hardware implementation testbench for Layer 2 IAB network and direct link between gNodeB-to-UE connection.

equalizer, PT-RS signals are equalized to mitigate the channel and noise effects. Employing  $\mathbf{NR}_{\text{Es}}^{\text{LS}}(\cdot)$  function, we can estimate the residual channel at the PT-RS locations in the  $\mathbf{R}_x^{\text{sub}}$  slot. Later on, one sum estimates across subcarriers is performed and after that the  $\hat{\theta}$  value is computed using the angle of the resultant sum as defined in (19). Finally, each OFDM symbol is corrected employing the  $\hat{\theta}$  value as observed in Algorithm 3.

In the last step in Algorithm 3, we execute the decoding of control, physical, and data channels, as well as determining other reference signals of the 5G downlink signal in time ( $n_{\text{sl}}$ ). Furthermore, LDPC technique has been considered in DL-SCH decoding. The estimated symbols and estimated bits are obtained and stores in  $\hat{\mathbf{y}}_{\text{UE}}^{\text{s}}$  and  $\hat{\mathbf{y}}_{\text{UE}}^{\text{b}}$ , respectively. Thus, in the **KPIs** block from the proposed UE block diagram is performed, and obtained the metrics to compare the direct link and access link performance.

## V. MEASUREMENTS CAMPAIGNS AND SIGNAL PARAMETERS

In this section, we define the experimental scenario of the hardware implementation testbench for the Layer 2 cooperative 5G network proposed in this paper. Field trial tests are conducted in a local area and shown in Fig. 10. There are three typical scenarios where the UE node receives signal. In the 5G network-based downlink IAB architecture proposed,  $N_{\text{T}}^{\text{S}} = N_{\text{R}}^{\text{R}} = N_{\text{T}}^{\text{R}} = N_{\text{T}}^{\text{D}} = 1$  antennas are

considered. The established channel between each node in the developed network occurred in an indoor propagation environment.

The experiments were carried out in the fourth floor of building C of the E.T.S.I de Telecomunicación, Universidad Politécnica de Madrid (UPM). The measurements were performed in an indoor-to-indoor hall and its layout is shown in Fig. 10. It can be seen in Fig. 10 that gNodeB presents NLOS propagation channels with respect to the UE positions. In addition, we have established the most critical deployments of the D&F protocol positions where NLOS propagation channels are dominant in the communication with the gNodeB (backhaul link) providing greater flexibility for the IAB network in terms of deployment, as they do not require direct visibility between the Layer 2 protocol and the gNodeB. It should be highlighted that we have defined two scenarios, firstly we have placed a Layer 2 protocol to 3.61 m and with NLOS channel with respect to the Base Station (D&F farthest, as defined in Fig. 10). The D&F farthest is placed at 6.54 m with respect to UE positions and has a LOS environment. On the other hand, the second scenario considers the D&F nearest which was placed 4.67 m from the gNodeB with NLOS propagation channel established between them. Furthermore, the UE positions have a LOS channel with respect to the D&F nearest and the distance between them is approximately 5.76 m. Finally, in both scenarios, the gNodeB was placed 9.14 m away from the UE positions.

**TABLE 1.** Main parameters to implement the FR1 and FR2 5G signals.

Parameters	FR1 5G signal	FR2 5G signal
$F_s$	10 MHz	50 MHz
Carrier Frequency, $f_s$	3.5 GHz	60 GHz
Tx/Rx Schemes	SISO	SISO
5G Duplex Scheme	NR-FDD	NR-FDD
Modulation	64-QAM	Q-PSK
Target Code Rate	3/4	1/3
Samples Rate	15.36 MHz	61.44 MHz
Cyclic Prefix	Normal	Normal
Number of FFT	1024	1024
Allocated RBs	52	66
Subcarriers $\times$ RB	12	12
$N_{\text{slot}}^{\text{slot}}$	14	14
Slots $\times$ Subframe	1	4
$n_f^{\mu}$	10	40
SS/PBCH Block	slot 0	slot 0
Subcarrier Spacing	15 kHz	120 kHz
Number of Cell ID	0	0
Max. Throughput	23.05 Mbps	19.02 Mbps
Transmission	20	20
Frames $\times$ Transmission	80	80

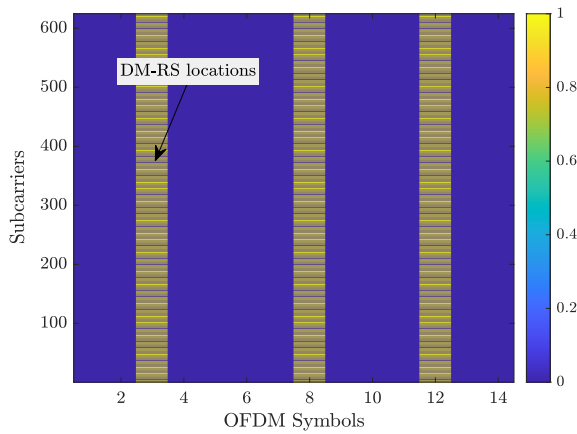
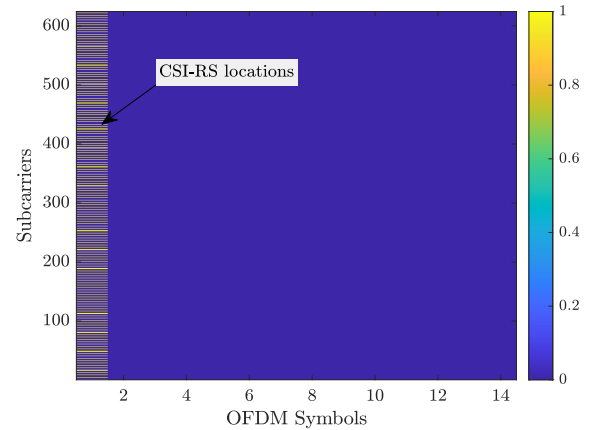
**FIGURE 11.** DM-RS time-frequency mapping to physical resource locations.

Table 1 reports the main parameters of interest concerning the developed hardware platform. In the table, the FR1 5G signal column details the parameters corresponding to the emulated signal in the gNodeB node. An FR1 5G downlink signal with a subcarrier spacing of 15 kHz, a sampling rate of 15.36 MHz, and a carrier frequency of 3.5 GHz has been considered. It is worth mentioning that, 23.05 Mbps is the maximum throughput that can be achieved by the UE when the direct link is established depending on the propagation channel conditions. On the other hand, the FR2 5G signal is the developed signal in the Layer 2 protocol transmitter-side. It can be seen that an FR2 signal with 50 MHz bandwidth has been implemented with a sampling frequency of 61.44 MHz. It should be highlighted that the FR2 signal configuration supports 4 slots per subframe and 40 slots per frame as shown in Table 1. Furthermore, the throughput maximum is 19.02 Mbps to the Q-PSK modulation scheme and a 1/3 target code rate. Note that several transmissions (20) have been performed from the base station and Layer 2 protocol and for each transmission 80 frames are sent.

**FIGURE 12.** CSI-RS time-frequency mapping to physical resource locations.

Considering the proposed reference signals to obtain the pilot samples in Subsection III-A and to perform the LS channel estimation, in this subsection we define the main parameters implemented in the Layer 2 protocol to execute each algorithm. Firstly, the DM-RS pilot samples are detailed where the demodulation reference signal type position 2 has been considered. Besides, the length was defined as 1 and an additional position of 2 is implemented. Configuration type, port set, and the number of DM-RS CDM groups without data are configured with 1, 1, and 2 values, respectively. Finally,  $N_{ID}^0 = N_{ID}^1 = 1$  and  $n_{SCID} = 0$  have been taken in the implementation. Thus, the generated DM-RS sequence is mapped to physical resources considering the parameters above related and it is allocated as illustrated in Fig. 11.

CSI-RS signal in (14) is defined as 3GPP [37] and the parameter values for its implementation in our platform are now introduced. The CSI-RS is configured for non-zero power with a density equal to 3, the primary use of which is to perform channel measurement. NZP CSI-RS is implemented to cover the whole part of the bandwidth (allocated RBs = 52) whose row number is equal to 1. The subcarrier locations and scrambling are defined with 0 and 1 values, respectively. Lastly, doing better channel estimation CSI-RS resource has been configured to be presented in all slots. Once defined the parameters, pilot symbols to perform practical channel estimation NZP CSI-RS has been obtained and mapped in the physical resources as shown in Fig. 12.

As presented in the proposed experimental scenario in Fig. 10, the access link is established in the mmWave band through the Pasternack's 60 GHz transmitter and receiver waveguide modules as has been explained in the implemented testbench in Fig. 3. This work implements a phase noise cancellation algorithm considering the PT-RS signals as detailed in Subsection III-B, in this sense, the following lines are devoted to define the main parameters that have been considered in our implementation. The radio network temporary identifier ( $n_{RNTI}$ ) is defined as 1, as well as the allocated RBs  $N_{RB} = 66$ . The frequency density  $K_{PT-RS} = 2$

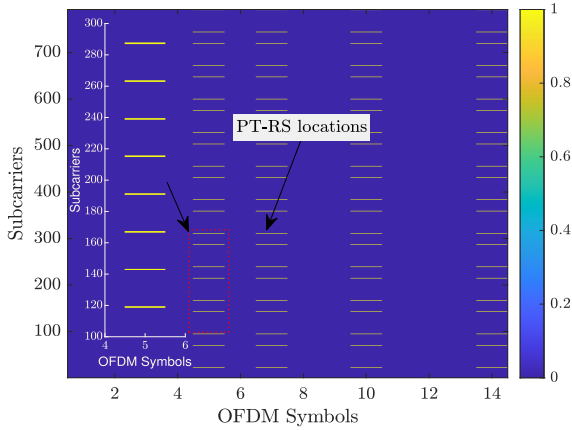


FIGURE 13. PT-RS time-frequency mapping to physical resource locations.

has been implemented. A time density with a value equal to 2 has been designed to control the time resources of the PT-RS signals. The parameter  $k_{\text{ref}}^{\text{RE}}$  is parameterized as 8 and it has been calculated by means of the DM-RS configuration type 1 and the resource element offset 11. Considering the above assumption, in this work, the PT-RS for the mmWave access link is mapped as described in Fig. 13.

## VI. NUMERICAL ANALYSIS AND DISCUSSIONS

In order to verify the Layer 2 protocol performance of the proposed IAB architecture for the 5G network, this section presents and discusses the main results obtained under the real-world environment presented in the previous section. First, the performance of the DM-RS and CSI-RS pilot samples for the LS estimator implementation into the Layer 2 protocol is compared. In this section, we also evaluate the performance of the proposed flexible mmWave Layer 2 protocol implementation for IAB architecture. In addition, we provide a comparison between the IAB architecture for a 5G system and a traditional 5G network with detailed explanations for each result obtained.

### A. LS ESTIMATOR PERFORMANCE CONSIDERING DM-RS AND CSI-RS SIGNALS

This subsection assesses the impact of channel estimation on the proposed Layer 2 protocol performance. In Fig. 14, we present the absolute value of estimated channel coefficients as a spectrogram plot for all the resource elements in the data channel grid considering the LS DM-RS and LS CSI-RS estimators when the D&F farthest is taken into account. Then, Fig. 15 illustrates the absolute value of estimated channel coefficients as a spectrogram plot for all the resource elements in the data channel grid considering the LS DM-RS and LS CSI-RS estimators when the D&F nearest is considered as the experimental environment. From the figures, it can be observed that there exists a variation in the channel coefficients across the data channel grid in the form of a 2D image, where the absolute value of channel estimates is color-coded in a heat map.

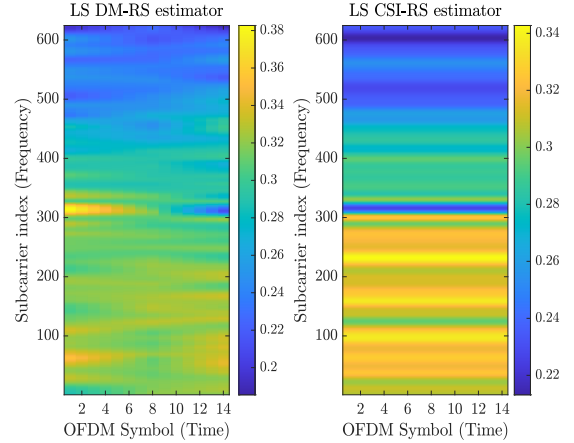


FIGURE 14. Spectrogram plot of the absolute value of the channel coefficient for the LS DM-RS and LS CSI-RS estimators in the D&F farthest environment.

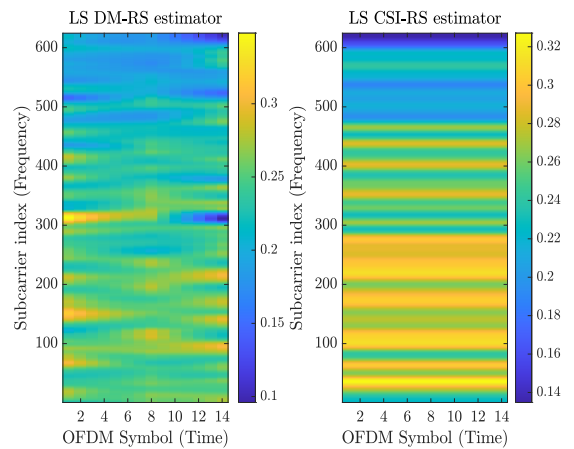
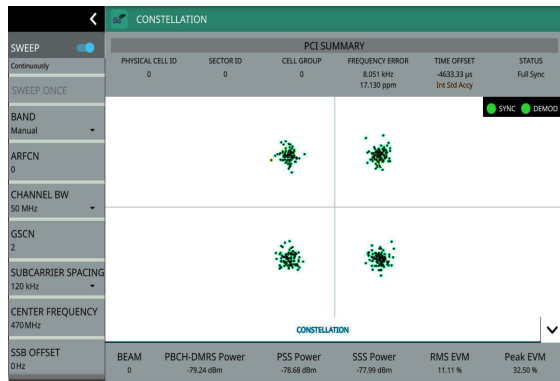


FIGURE 15. Spectrogram plot of the absolute value of the channel coefficient for the LS DM-RS and LS CSI-RS estimators in the D&F nearest environment.

Table 2 presents the channel estimation performance comparison between the LS estimator with DM-RS pilot samples and LS with CSI-RS pilot symbols considering the experimental scenarios described in Section V. The experimental results show that the error vector magnitude of the 64-QAM modulation scheme in the data channel is lower when the D&F farthest is considered in both channel estimation algorithms, which is due to the distance. Nevertheless, in the backhaul link in the D&F nearest scenario is higher than in the D&F farthest experimental environment. So, let assumed the D&F nearest environment, in this case, it can be observed from the table that the EVM of LS DM-RS is 2.7% lower than the LS CSI-RS algorithm. It can be seen that the Time $\times$ Symbols is lower in the LS CSI-RS. This small difference is due to the fact that in the LS CSI-RS fewer symbols are mapped in the resource grid as shown in Fig. 12. It is worth noting that several experimental results were obtained where we found that the main difference in the EVM between the LS DM-RS and LS CSI-RS estimators is

**TABLE 2.** Performance evaluation of LS DM-RS and LS CSI-RS estimators under the proposed experimental environments.

Metrics	LS DM-RS		LS CSI-RS	
	Farthest	Nearest	Farthest	Nearest
PDSCH EVM [%]	10.11	15.77	15.51	18.47
Time×Symbols [ $\mu$ s]	1.2788	1.2949	1.1053	1.1061

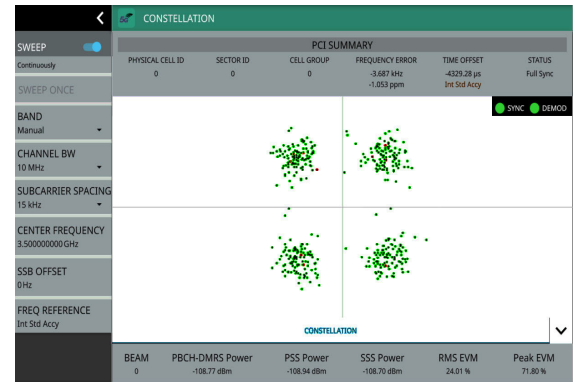
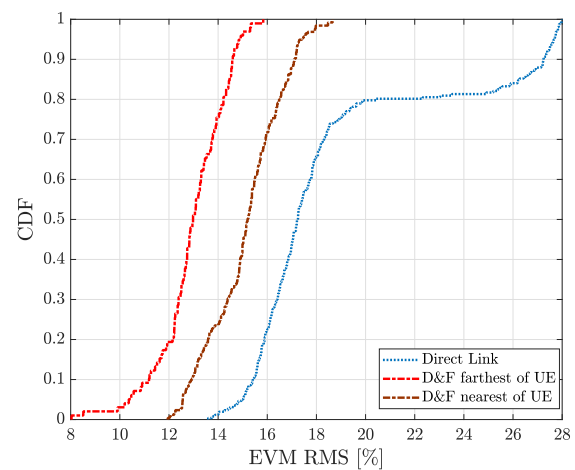
**FIGURE 16.** Demodulation of the mmWave access link signal in the UE positions.

due to the fact that there are more pilot symbols in the former algorithm.

### B. SYSTEM-LEVEL EVALUATION OF IAB ARCHITECTURE

In order to verify the performance of the proposed Layer 2 protocol and IAB network implementation, extensive measurements have been performed using the Anritsu equipment allowing to demonstrate that our platform supports 5G signal, both FR1 and FR2, standardized by the 3GPP. Considering the first scenario that takes into account the D&F farthest, Fig. 16 shows the demodulation of the synchronization/PBCH block of the FR2 received signal from the Layer 2 protocol in the UE positions. It can be observed in the left menu that the parameters demodulated in the commercial equipment correspond to the ones defined in Section V (50 MHz bandwidth, 120 kHz subcarrier spacing, and 470 MHz center frequency in baseband after the Paster-nack receiver). In addition, the direct link has been measured for comparison and is presented in Fig. 17.

From the results presented in Figs. 16 and 17 we conclude that in both cases a full synchronization and demodulation (physical Cell ID is 0, as defined in Section V) between the equipment and the received signal is performed. The measurements from Fig. 16 shows the EVM of the broadcast channel, which is approximately 11%. When compared to the signal obtained from the direct link in Fig. 17, the EVM of the broadcast channel is considerably low. Besides, the value obtained is lower than the one standardized by the 3GPP for the Q-PSK modulation scheme (18%). It should be highlighted that the SSB demodulation was also performed using the same algorithms developed in the UE node and the mean results are close to the obtained in the Anritsu equipment, indicating a similar performance.

**FIGURE 17.** Demodulation of the sub-6 GHz direct link signal in the UE positions.**FIGURE 18.** PBCH performance of UE node through implemented IAB architecture for 5G network based on mmWave Layer 2 protocol.

The EVM [%] performance of the physical broadcast channel decoded at the UE node via the direct link and the access link is shown in Fig. 18. The measurements of the broadcast channel by means of the IAB architecture were performed using the D&F nearest and D&F farthest environments, as exhibited in Fig. 18. The EVM measurement results with the 5G traditional network is noteworthy high, achieving 27.24% of error for 90% of the time. Compared with the measurement results of the developed IAB architecture, the EVM results through the proposed Layer 2 protocol degraded significantly by approximately 10.07% and 12.64%, respectively, when considering the D&F nearest and D&F furthest scenarios. Furthermore, the above explanation demonstrates the great benefit of the IAB architecture for 5G networks. Besides, the difference in EVM characteristics between the Layer 2 protocol positions can be seen in Fig. 18, achieving the best performance when the D&F furthest is taken into account, despite a longer distance in comparison with the D&F nearest. It should be noted that this result is due to the fact that the Layer 2 protocol in the D&F farthest scenario has a high perpendicularity with respect to the UE node positions. On the other hand, comparing the obtained



**TABLE 3.** Mean bit error rate of the implemented architectures.

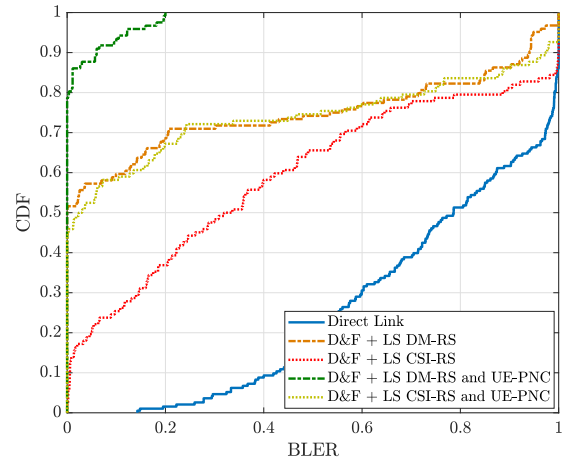
Architectures	Scenarios	
	Farthest	Nearest
D&F + LS DM-RS	$2.68 \times 10^{-3}$	$9.68 \times 10^{-3}$
D&F + LS CSI-RS	$1.43 \times 10^{-2}$	$7.22 \times 10^{-2}$
D&F + LS DM-RS and UE-PNC	$1.23 \times 10^{-4}$	$0.97 \times 10^{-3}$
D&F + LS CSI-RS and UE-PNC	$7.69 \times 10^{-3}$	$9.12 \times 10^{-3}$
Direct Link	$9.97 \times 10^{-2}$	

results through Anritsu equipment and our proposed platform for both direct link and IAB architecture, we concluded that a similar performance is achieved.

Table 3 illustrates the UE mean bit error rate (BER) of the implemented architectures considering a Q-PSK modulation in the access link (transmission from the mmWave Layer 2 protocol) and a 64-QAM modulation in the direct link. It can also be noticed that the nearest and farthest scenarios have been taken into considered, as well as communication by means of the direct link has been employed in the comparison. From the table, we can see that the BER of the proposed IAB architecture increases when contemplating the nearest environment. However, compared to the proposed IAB architecture, the conventional downlink 5G network suffers from a significant performance loss due to the propagation channel conditions. The performance of the IAB architecture using the mmWave Layer 2 protocol with the LS DM-RS estimator achieves a lower error than the mmWave Layer 2 protocol with the LS CSI-RS algorithm, e.g., in the furthest environment, the platform implemented with the Layer 2 protocol with the LS DM-RS algorithm achieves a  $1.16 \times 10^{-2}$  lower error than in the LS CSI-RS case. Finally, from Table 3 we can conclude that the lowest errors were achieved when the proposed phase noise cancellation algorithm was introduced at the UE node where the best performance is obtained with the mmWave Layer 2 protocol with LS DM-RS and UE-PNC scheme and its value is  $1.23 \times 10^{-4}$  under the farthest scenario.

The block error rate (BLER) is defined as the ratio of the number of transport blocks received in error to the total number of blocks transmitted over a certain number of frames, considering that 80 frames are sent in each transmission. This metric has been obtained after channel de-interleaving and decoding by evaluating the cyclic redundancy check (CRC) in each received transport block. It can be seen in Fig. 19 that the BLER performance of the direct link communication is significantly higher than in the link adopting the D&F protocol, showing the advantage of the proposed Layer 2 protocol. For example, the UE connection through the direct link reaches 0.88 block probability for 60% of the cases translating into a low available capacity.

It can be observed that by considering the proposed Layer 2 protocol in the IAB network the error of the UE decreases enormously. In the case of the scenario with D&F with LS CSI-RS algorithm, the BLER probability in the UE was 0.44 for 60% of the time reaching a reduction of 0.44 block


**FIGURE 19.** BLER of proposed out-of-band mmWave Layer 2 protocol considering the D&F farthest scenario.

probability. So, when considered the Layer 2 protocol with LS CSI-RS and UE with PNC technique the measured results exhibits a BLER of 0.13 for 60% of the time being decreased 0.75 and 0.31 when compared to the direct link and D&F protocol with LS CSI-RS estimator, respectively. However, by performing a comparison of the Layer 2 protocol in the LS DM-RS and LS CSI-RS estimators, we observe that the BLER in UE is significantly lower when using the LS DM-RS algorithm, which is reached a 0.09 for 60% of the time. In addition, it should be noted that the BLER achieved by the IAB architecture using the Layer 2 protocol with LS DM-RS algorithm is lower than the Layer 2 protocol with LS CSI-RS estimator and UE with PNC algorithm, as shown in Fig. 19. Finally, from the experimental results shown in Fig. 19 we can conclude that the best performance was achieved when the IAB architecture has been taken into account for the 5G network using Layer 2 protocol with LS DM-RS estimator and UE node with PNC scheme in which a value of 0.0036 is achieved for 80% of the time at the UE node.

We used the D&F nearest environment to evaluate the implemented IAB architecture based on the proposed mmWave Layer 2 protocol. Fig. 20 shows the BLER reached by the UE node with our implemented traditional 5G network and the proposed IAB architecture. In Fig. 20, we observe that the implemented architectures present the same behavior as the results obtained in Fig. 19. In this context, BLER degradation is caused by the propagation channel environment. For example, the lowest BLER is approximately 0.059 for the 60% of the time, and however with the presented results in Fig. 19, a 0 value is achieved for the 60% of the time using the same architecture, i.e., the IAB architecture based on mmWave Layer 2 protocol with LS DM-RS estimator and UE node with PNC algorithm.

The experimental results of the hardware IAB architecture for 5G network using mmWave out-of-band Layer 2 protocol are given for two propagation channel conditions, as can be

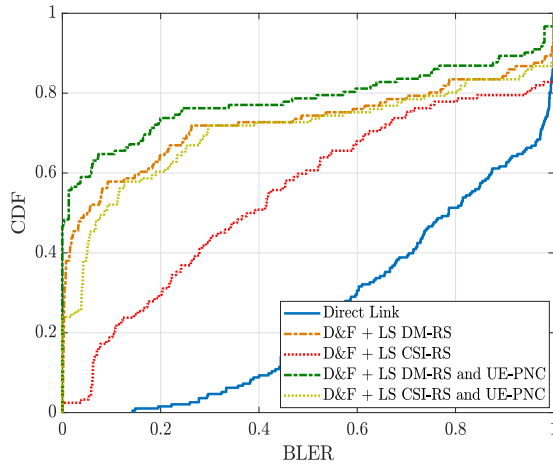


**FIGURE 20.** BLER of proposed out-of-band mmWave Layer 2 protocol considering the D&F nearest scenario.

**TABLE 4.** Throughput performance of the proposed IAB architecture and comparison with the traditional 5G network.

Architectures	Throughput [Mbps]		$C_L$ [%]	
	Farthest	Nearest	Farthest	Nearest
D&F + LS DM-RS	14.86	12.22	21.89	35.76
D&F + LS CSI-RS	9.82	7.52	48.38	60.47
D&F + LS DM-RS and UE-PNC	18.89	15.54	0.70	18.31
D&F + LS CSI-RS and UE-PNC	13.84	11.16	27.45	41.34
Direct Link	5.73		75.14	

found in Table 4. It can be shown that the Layer 2 protocol with LS CSI-RS estimator achieved a capacity of 7.52 Mbps under the nearest environment, however, the Layer 2 protocol with LS DM-RS algorithm increases the throughput performance by 7.34 Mbps in the same environment. The maximum capacity of the Layer 2 protocol with LS CSI-RS estimator was 13.84 Mbps when considering the UE node with PNC algorithm and under the farthest propagation channel environment. When the Layer 2 protocol with LS DM-RS estimator and UE node with PNC algorithm under the nearest environment was taken into consideration, the UE node reached 15.54 Mbps, implying that a 3.32 Mbps and 4.38 Mbps were successfully achieved compared with the Layer 2 protocol with LS DM-RS algorithm and Layer 2 protocol with LS CSI-RS scheme and UE node with PNC algorithm in the nearest environment, respectively. It should be highlighted that the reached higher throughput performance was 18.89 Mbps by means of the IAB architecture employing the mmWave Layer 2 protocol with LS DM-RS estimator and UE node with PNC algorithm under the farthest scenario which compared with the direct link communication a gain performance of 13.16 Mbps was achieved.

In the following, we focus on determining the throughput loss in each one implemented architectures depending on the throughput maximum standardized by the 3GPP, we defined

the  $C_L$  [%] metric as

$$C_L[\%] = 100 \times \frac{(C_{Max} - C_{Obt})}{C_{Max}}, \quad (23)$$

where the  $C_{Max}$  is the maximum throughput standardized by the 3GPP depending on the modulation scheme and modulation coding index (the maximum throughput without any propagation channel for 64-QAM modulation scheme in FR1 5G signal and Q-PSK constellation scheme in FR2 5G signal have been described in Table 1) and  $C_{Obt}$  depicts the obtained throughput. Table 4 also illustrate the  $C_L$  results obtained through the expression (23). From the experimental measurements, it can be observed that the direct link communication achieved the highest  $C_L$  with approximately a 75.14% which can be computed by means of (23) considering  $C_{Max} = 23.05$  Mbps and  $C_{Obt} = 5.73$  Mbps. However, among the implemented IAB architectures, the best results were obtained when considering the PNC algorithm and the LS DM-RS estimator in the mmWave out-of-band Layer 2 protocol. In this context, we observe that a 0.70% ( $100 \times \frac{(19.02 - 18.89)}{19.02}$ ) of capacity loss was achieved when the farthest environment was taken into consideration.

## VII. CONCLUSION

In this paper, we have presented an out-of-band IAB hardware architecture for the 5G communication network, focusing on the design and implementation of the baseband algorithms and RF front-end integration of the mmWave Layer 2 protocol. Based on the 3GPP standard, we implemented the LS channel estimator through the DM-RS and CSI-RS pilot samples into the Layer 2 protocol. Considering that phase noise introduces a huge performance deterioration in the mmWave communication system, we implemented a phase noise cancellation algorithm that introduces the phase tracking reference signals into the transmitted FR2 signal of the mmWave Layer 2 protocol to help jointly compensate for the phase noise in the reception. We conclude that the implemented IAB architecture using mmWave Layer 2 protocol is a 5G enabling that has the potential to improve the throughput, EVM, BLER, and BER of the users in the indoor environments. Test results reveal that the proposed protocol and IAB network support FR1 and FR2 real-5G downlink signals and the obtained measures are similar to the presented with Anritsu equipment. Our experimental results have demonstrated that the implemented IAB architecture based on the proposed Layer 2 protocol with LS DM-RS estimator and UE with PNC algorithm can achieve better KPIs than the conventional 5G network. The main limitation of the proposed IAB architecture is the need of LOS between both horn antennas in the mmWave access link, as NLOS severely degrades its performance. This limitation opens a new implementation paradigm where a circularly polarized radial line patch array antenna allowing the steering of the main beam can be designed to improve the IAB performance and overcome the limitations of the mmWave link. In addition, the proposed IAB platform is considered a flexible implementation that will integrate

another mmWave communication system in the backhaul link operating in the frequency range 24–28 GHz. This allows the adoption of a FR1 or a FR2 backhaul link and address other aspects not taken into consideration in this work, including a comparison in terms of performance, complexity, and cost. Finally, we believe that the designed platform provides a cost-effective, scalable, and easy-to-upgrade solution for enabling other 5G signals standardized by the 3GPP, as well as, novel 5G as MIMO, beamforming techniques, and deep-learning based approach [49] in mmWave frequency bands.

## REFERENCES

- [1] O. O. Erunkulu, A. M. Zungeru, C. K. Lebekwe, M. Mosalaosi, and J. M. Chuma, "5G mobile communication applications: A survey and comparison of use cases," *IEEE Access*, vol. 9, pp. 97251–97295, 2021.
- [2] A. Gupta and R. K. Jha, "A survey of 5G network: Architecture and emerging technologies," *IEEE Access*, vol. 3, pp. 1206–1232, 2015.
- [3] Y. Prathyusha and T. Sheu, "Coordinated resource allocations for eMBB and URLLC in 5G communication networks," *IEEE Trans. Veh. Technol.*, vol. 71, no. 8, pp. 8717–8728, Aug. 2022.
- [4] A. A. Esswie and K. I. Pedersen, "Opportunistic spatial preemptive scheduling for URLLC and eMBB coexistence in multi-user 5G networks," *IEEE Access*, vol. 6, pp. 38451–38463, 2018.
- [5] X. Song and M. Yuan, "Performance analysis of one-way highway vehicular networks with dynamic multiplexing of eMBB and URLLC traffics," *IEEE Access*, vol. 7, pp. 118020–118029, 2019.
- [6] M. Almekhlafi, M. A. Arfaoui, M. Elhattab, C. Assi, and A. Ghayeb, "Joint resource allocation and phase shift optimization for RIS-aided eMBB/URLLC traffic multiplexing," *IEEE Trans. Commun.*, vol. 70, no. 2, pp. 1304–1319, Feb. 2022.
- [7] L. Tong, C. Zhang, and R. Huang, "Research on intelligent logic design and application of campus MMTC scene based on 5G slicing technology," *China Commun.*, vol. 18, no. 8, pp. 307–315, Aug. 2021.
- [8] K. Mikhaylov, V. Petrov, R. Gupta, M. A. Lema, O. Galinina, S. Andreev, Y. Koucheryavy, M. Valkama, A. Pouttu, and M. Dohler, "Energy efficiency of multi-radio massive machine-type communication (MR-MMTC): Applications, challenges, and solutions," *IEEE Commun. Mag.*, vol. 57, no. 6, pp. 100–106, Jun. 2019.
- [9] D. He, B. Ai, K. Guan, L. Wang, Z. Zhong, and T. Kürner, "The design and applications of high-performance ray-tracing simulation platform for 5G and beyond wireless communications: A tutorial," *IEEE Commun. Surveys Tuts.*, vol. 21, no. 1, pp. 10–27, 1st Quart., 2019.
- [10] F. Hamidi-Sepehr, M. Sajadieh, S. Pantelev, T. Islam, I. Karls, D. Chatterjee, and J. Ansari, "5G URLLC: Evolution of high-performance wireless networking for industrial automation," *IEEE Commun. Standards Mag.*, vol. 5, no. 2, pp. 132–140, Jun. 2021.
- [11] M. Giordani, M. Polese, A. Roy, D. Castor, and M. Zorzi, "A tutorial on beam management for 3GPP NR at mmWave frequencies," *IEEE Commun. Surveys Tuts.*, vol. 21, no. 1, pp. 173–196, 1st Quart., 2019.
- [12] I. A. Hemadeh, K. Satyanarayana, M. El-Hajjar, and L. Hanzo, "Millimeter-wave communications: Physical channel models, design considerations, antenna constructions, and link-budget," *IEEE Commun. Surveys Tuts.*, vol. 20, no. 2, pp. 870–913, 2nd Quart., 2018.
- [13] S. Dinh-Van, T. M. Hoang, B. B. Cebecioglu, D. S. Fowler, Y. K. Mo, and M. D. Higgins, "A defensive strategy against beam training attack in 5G mmWave networks for manufacturing," *IEEE Trans. Inf. Forensics Security*, vol. 18, pp. 2204–2217, 2023.
- [14] K. Hassan, M. Masarra, M. Zwingelstein, and I. Dayoub, "Channel estimation techniques for millimeter-wave communication systems: Achievements and challenges," *IEEE Open J. Commun. Soc.*, vol. 1, pp. 1336–1363, 2020.
- [15] J. Huang, Y. Liu, C. Wang, J. Sun, and H. Xiao, "5G millimeter wave channel sounders, measurements, and models: Recent developments and future challenges," *IEEE Commun. Mag.*, vol. 57, no. 1, pp. 138–145, Jan. 2019.
- [16] S. He, Y. Zhang, J. Wang, J. Zhang, J. Ren, Y. Zhang, W. Zhuang, and X. Shen, "A survey of millimeter-wave communication: Physical-layer technology specifications and enabling transmission technologies," *Proc. IEEE*, vol. 109, no. 10, pp. 1666–1705, Oct. 2021.
- [17] T. Ferreira, A. Figueiredo, D. Raposo, M. Luís, P. Rito, and S. Sargento, "Millimeter-wave feasibility in 5G backhaul: A cross-layer analysis of blockage impact," *IEEE Access*, vol. 11, pp. 5178–5192, 2023.
- [18] 5G; NR; Study on Integrated Access and Backhaul, Standard 3GPP TS 38.874, Rel. 16, 3GPP, 2018.
- [19] Y. Cai, Y. Xu, Q. Shi, B. Champagne, and L. Hanzo, "Robust joint hybrid transceiver design for millimeter wave full-duplex MIMO relay systems," *IEEE Trans. Wireless Commun.*, vol. 18, no. 2, pp. 1199–1215, Feb. 2019.
- [20] U. Siddique, H. Tabassum, and E. Hossain, "Downlink spectrum allocation for in-band and out-band wireless backhauling of full-duplex small cells," *IEEE Trans. Commun.*, vol. 65, no. 8, pp. 3538–3554, Aug. 2017.
- [21] J. Suomalainen, J. Julku, M. Vehkaperä, and H. Posti, "Securing public safety communications on commercial and tactical 5G networks: A survey and future research directions," *IEEE Open J. Commun. Soc.*, vol. 2, pp. 1590–1615, 2021.
- [22] K. Ali, H. X. Nguyen, Q. Vien, P. Shah, M. Raza, Vishnu, V. Paranthaman, B. Er-Rahmadi, M. Awais, S. u. Islam, and J. J. P. C. Rodrigues, "Review and implementation of resilient public safety networks: 5G, IoT, and emerging technologies," *IEEE Netw.*, vol. 35, no. 2, pp. 18–25, Mar. 2021.
- [23] X. Lin, "An overview of 5G advanced evolution in 3GPP release 18," *IEEE Commun. Standards Mag.*, vol. 6, no. 3, pp. 77–83, Sep. 2022.
- [24] Z. Xiao, P. Xia, and X. Xia, "Full-duplex millimeter-wave communication," *IEEE Wireless Commun.*, vol. 24, no. 6, pp. 136–143, Dec. 2017.
- [25] B. De Beelde, M. Vantorre, G. Castellanos, M. Pickavet, and W. Joseph, "MmWave physical layer network modeling and planning for fixed wireless access applications," *Sensors*, vol. 23, no. 4, p. 2280, Feb. 2023.
- [26] M. Polese, M. Giordani, T. Zugno, A. Roy, S. Goyal, D. Castor, and M. Zorzi, "Integrated access and backhaul in 5G mmWave networks: Potential and challenges," *IEEE Commun. Mag.*, vol. 58, no. 3, pp. 62–68, Mar. 2020.
- [27] M. Polese, M. Giordani, A. Roy, D. Castor, and M. Zorzi, "Distributed path selection strategies for integrated access and backhaul at mmWaves," in *Proc. IEEE Global Commun. Conf. (GLOBECOM)*, Dec. 2018, pp. 1–7.
- [28] C. Madapatha, B. Makki, C. Fang, O. Teyeb, E. Dahlman, M. Alouini, and T. Svensson, "On integrated access and backhaul networks: Current status and potentials," *IEEE Open J. Commun. Soc.*, vol. 1, pp. 1374–1389, 2020.
- [29] J. Zhang, H. Luo, N. Garg, A. Bishnu, M. Holm, and T. Ratnarajah, "Design and analysis of wideband in-band-full-duplex FR2-IAB networks," *IEEE Trans. Wireless Commun.*, vol. 21, no. 6, pp. 4183–4196, Jun. 2022.
- [30] S. H. R. Naqvi and P. Ho, "Achieving 5G NR mmWave indoor coverage under integrated access backhaul," *IEEE Syst. J.*, vol. 15, no. 4, pp. 5429–5439, Dec. 2021.
- [31] C. Huang, X. Wang, and X. Wang, "Effective-capacity-based resource allocation for end-to-end multi-connectivity in 5G IAB networks," *IEEE Trans. Wireless Commun.*, vol. 21, no. 8, pp. 6302–6316, Aug. 2022.
- [32] Á. Hernández-Solana, P. García-Dúcar, A. Valdovinos, J. E. García, J. D. Mingo, and P. L. Carro, "Experimental evaluation of transmitted signal distortion caused by power allocation in inter-cell interference coordination techniques for LTE/LTE-A and 5G systems," *IEEE Access*, vol. 10, pp. 47854–47868, 2022.
- [33] E. Coronado, S. N. Khan, and R. Riggio, "5G-EmPOWER: A software-defined networking platform for 5G radio access networks," *IEEE Trans. Netw. Service Manage.*, vol. 16, no. 2, pp. 715–728, Jun. 2019.
- [34] R. Verdecia-Peña and J. I. Alonso, "Design and synchronization procedures of a D&F co-operative 5G network based on SDR hardware interface: Performance analysis," *Sensors*, vol. 22, no. 3, p. 913, Jan. 2022.
- [35] M. Chung, H. Prabhu, F. Sheikh, O. Edfors, and L. Liu, "Low-complexity fully-digital phase noise suppression for millimeter-wave systems," in *Proc. IEEE Int. Symp. Circuits Syst. (ISCAS)*, Oct. 2020, pp. 1–5.
- [36] M. Chung, L. Liu, and O. Edfors, "Phase-noise compensation for OFDM systems exploiting coherence bandwidth: Modeling, algorithms, and analysis," *IEEE Trans. Wireless Commun.*, vol. 21, no. 5, pp. 3040–3056, May 2022.
- [37] 5G; NR; Physical Channels and Modulation, Standard 3GPP 5G TS38.211 v.16.2.0 Release 16, 2020.
- [38] 5G; System Architecture for the 5G System (5GS), Standard 3GPP 5G TS38.300 v.17.4.0 Release 17, 2022.
- [39] W. Chen, J. Montojo, J. Lee, M. Shafi, and Y. Kim, "The standardization of 5G-advanced in 3GPP," *IEEE Commun. Mag.*, vol. 60, no. 11, pp. 98–104, Nov. 2022.
- [40] 5G; NR; Base Station (BS) Radio Transmission and Reception, Standard 3GPP 5G TS38.104 v.15.2.0 Release 15, 2018.

- [41] Pasternack Transceiver. *60 GHz Development System*. Accessed: Sep. 3, 2021. [Online]. Available: <https://www.pasternack.com/images/ProductPDF/PEM009-KIT.pdf>
- [42] Y. Zhang, J. Liu, S. Feng, and P. Zhang, "Pilot design for phase noise mitigation in millimeter wave MIMO-OFDM systems," in *Proc. IEEE 85th Veh. Technol. Conf. (VTC Spring)*, Jun. 2017, pp. 1–6.
- [43] D. Petrovic, W. Rave, and G. Fettweis, "Effects of phase noise on OFDM systems with and without PLL: Characterization and compensation," *IEEE Trans. Commun.*, vol. 55, no. 8, pp. 1607–1616, Aug. 2007.
- [44] T. Levanen, O. Tervo, K. Pajukoski, M. Renfors, and M. Valkama, "Mobile communications beyond 52.6 GHz: Waveforms, numerology, and phase noise challenge," *IEEE Wireless Commun.*, vol. 28, no. 1, pp. 128–135, Feb. 2021.
- [45] S. Gu, H. Long, and Q. Li, "Phase noise estimation and compensation algorithms for 5G systems," in *Proc. Int. Conf. Commun. Syst. Netw.*, China, Jan. 2019, pp. 551–561.
- [46] D. W. K. Ng, M. Breiling, C. Rohde, F. Burkhardt, and R. Schober, "Energy-efficient 5G outdoor-to-indoor communication: SUDAS over licensed and unlicensed spectrum," *IEEE Trans. Wireless Commun.*, vol. 15, no. 5, pp. 3170–3186, May 2016.
- [47] H. Ronkainen, J. Edstam, A. Ericsson, and C. Östberg, "Integrated access and backhaul a new type of wireless backhaul in 5G," *Ericsson Technol. Rev.*, vol. 2020, no. 7, pp. 2–11, Jun. 2020.
- [48] R. A. Verdecia-Pe and J. I. Alonso, "Simulation and experimental study of a power amplifier behaviour to enhance relay node co-operative SDR platform: Performance analysis," in *Proc. IEEE 12th Annu. Comp. Commun. Workshop Conf. (CCWC)*, Las Vegas, NV, USA, Jan. 2022, pp. 889–894.
- [49] T. Ferreira, A. Figueiredo, D. Raposo, M. Luís, P. Rito, and S. Sargento, "Improving mmWave backhaul reliability: A machine-learning based approach," *Ad Hoc Netw.*, vol. 140, Mar. 2023, Art. no. 103050.



**RANDY VERDECIA-PEÑA** (Member, IEEE) was born in Mabay-Granma, Cuba, in 1991. He received the degree in telecommunications and electronics engineering from the Higher Polytechnic Institute Julio Antonio Mella, Universidad de Oriente, Santiago of Cuba, Cuba, in 2014, and the M.Sc. degree in electrical engineering from the Pontificia Universidade Católica do Rio de Janeiro (PUC-Rio), Brazil, in 2019. He is currently pursuing the Ph.D. degree with Universidad Politécnica

de Madrid (UPM).

From 2014 to 2017, he was with Telecommunications Company of Cuba (ETECSA) as a Specialist in telematics. He is currently with the Department of Information Processing and Telecommunications Center, UPM. His research interest includes solutions for the physical layer of the future fifth generation of mobile communication systems (5G) and their hardware implementation. He has involved in the 3GPP standard in the solutions of new generation networks. He is currently involved in the study of new technologies and their implementation in high-speed railways (HSR) for 5G and 6G communications. He has received a scholarship from the Science, Innovation and University Ministry, Spain, and the CAPES Scholarship from Education Ministry, Brazil, in 2017.



**RODOLFO OLIVEIRA** (Senior Member, IEEE) received the Licenciatura degree in electrical engineering from the Faculdade de Ciências e Tecnologia (FCT), Universidade Nova de Lisboa (UNL), Lisbon, Portugal, in 2000, the M.Sc. degree in electrical and computer engineering from the Instituto Superior Técnico, Technical University of Lisbon, in 2003, and the Ph.D. degree in electrical engineering from UNL, in 2009. From 2007 to 2008, he was a Visiting Researcher with the University of Thessaly. From 2011 to 2012, he was a Visiting Scholar with Carnegie Mellon University. He is currently with the Department of Electrical and Computer Engineering, UNL. He is also a Senior Researcher with the Instituto de Telecomunicações. His research interests include wireless communications, computer networks, and computer science. He serves on the editorial board of *Ad Hoc Networks* (Elsevier), *ITU Journal on Future and Evolving Technologies* (ITU J-FET), *IEEE OPEN JOURNAL OF THE COMMUNICATIONS SOCIETY*, and *IEEE COMMUNICATIONS LETTERS*.



**JOSÉ I. ALONSO** (Member, IEEE) received the degree in telecommunications engineering and the Ph.D. degree from the Universidad Politécnica de Madrid (UPM).

He began his career with Telettra España, S.A., as a Microwave Design Engineer. Then, he joined the Department of Signals, Systems, and Radio-communications, UPM, where he is currently a Full Professor. He has also involved in the development and radio planning of broadband point multipoint radio systems (LMDS) in millimeter frequencies and wireless and mobile communications systems (WiFi, WiMAX, TETRA, GSM-R, and LTE). He is currently involved in the study of the viability of the use of 5G communications for critical communications and operational and passenger services in rail environments; in particular, its potential applicability to the FRMCS, in co-operative communications in 5G systems, and the development of localization techniques based on femtocell LTE networks. He has participated in more than 90 research projects and contracts financed by national and international institutions and companies. He has authored more than 200 publications in scientific journals, symposium proceedings, seminars, and reports. In addition, he holds three patents. His research interests include the analysis and simulation of high-speed/high-frequency integrated circuits and their interconnections, and the computer-aided design and measurement of hybrid and GaAs monolithic microwave integrated circuits (MMICs) and their applications in the development and implementation of mobile, optical fiber, and communications systems.

...